J. Fluid Mech. (1985), *vol.* 153, *pp.* 275–312
Printed in Great Britain

Computation of inviscid incompressible flow with rotation

By ARTHUR RIZZI† AND LARS-ERIK ERIKSSON
FFA, The Aeronautical Research Institute of Sweden, S-161 11 Bromma, Sweden

(Received 3 January 1984 and in revised form 16 October 1984)

The standard hyperbolic methods used to solve the compressible Euler equations are not effective in the limit of incompressible flow. The sound waves dominate the system and it becomes poorly conditioned for numerical solution. For steady flow governed by the incompressible Euler equations, artificial compressibility is a technique that removes the troublesome sound waves. It leads to a hyperbolic system of equations that we solve by finite-volume differences centred in space, and explicit multistage time-stepping. The stability of this novel system is analysed, its allowable discontinuities are described, and appropriate far-field and solid-wall boundary conditions are introduced. Results are presented for both two- and three-dimensional flows, including vorticity shed from a delta wing. Whether vorticity is produced or not depends very strongly on the body geometry, the accuracy of the solution method, and the transient discontinuities that evolve in the flow field. The results are analysed for the total-pressure losses in the flow fields, and for the diffusion of the vortex sheets.

1. Introduction

The ability to obtain detailed information about incompressible flow fields by the numerical solution of a set of governing equations affords great utility to industrial designers of turbomachinery, internal ducts, and pumps, as well as transport vehicles, be they ocean-going ships, road vehicles or airplanes. Most of these applications involve flows having very high Reynolds numbers, and the potential equation first comes to mind as the suitable flow model. Many of the flows, however, possess substantial regions with rotation, one very common feature being the shedding of vorticity from sharp edges. Working with the potential model, one faces the cumbersome task of setting up vortex-sheet discontinuities in the field and then adjusting or fitting them to the surrounding flow. This requires prior knowledge of where the sheets begin, and becomes very complicated for all but the simplest situations. The alternative, especially when the vortex topology is complex or unknown, is to adopt the Euler equations as the flow model because they allow rotational flow everywhere, and vortical regions are 'captured' implicitly as an integral part of the solution.

The recent discovery that a vortex sheet can be generated and captured in the solution of a *compressible* flow field with separation from the leading edge of a delta wing at high angle of attack has stirred up a lot of activity in the development of numerical methods to solve the compressible Euler equations. Unfortunately these

† Also at Royal Institute of Technology, Stockholm.

methods do not work very well for an *incompressible* problem simply by setting the free-stream Mach number to a very small value, zero in the limit, because with decreasing Mach number the speed of the sound waves becomes much larger than the speed of convection. This increasing disparity in wave speeds causes the governing system of hyperbolic equations to be poorly conditioned, and the stability of the computation is greatly impaired. If, however, the interest is only in steady flow, artificial compressibility is one way round the difficulty, because this approach removes the sound waves from the system by prescribing a pseudotemporal evolution for the pressure which is hyperbolic and which converges to the true steady-state value. Our purpose here is to describe a rather general numerical method that takes the artificial-compressibility approach for solving the steady incompressible Euler equations. We show how it leads to a hyperbolic system, carry out a numerical study of its condition, set forth the CFL stability limit for the time integration, and examine the types of discontinuities that it admits. Appropriate numerical far-field and solid-wall boundary conditions are formulated also.

The central issues here, as for the compressible equations, are to understand how vorticity is created in the flow, to calibrate the diffusion of the vorticity, and to gauge to what extent errors in total pressure degrade the overall accuracy of the solution. We try to shed light on these computed solutions in comparison with the corresponding potential solutions that are accepted as being accurate. The first is the simplest, incompressible flow past a circle, for which the computed solution is irrotational and compares well with the analytical Laplace solution. The second is lifting flow around the NACA 0012 airfoil, and we observe how the correct circulation arises during the transient evolution of the flow. The last is flow past a flat-plate delta wing in which a stable vortex sheet is shed from the leading edge and then coils up into a steady vortex over the wing. We analyse the qualitative as well as quantitative aspects of this flow in comparison with the results of a 3-dimensional panel method that fits the vortex sheet to the surrounding potential-flow field.

2. Artificial-compressibility method

In this section the method for solving the Euler equations for incompressible flow is described. First a discussion of the mathematical model is presented, followed by a description of the computational method.

2.1. *Mathematical model*

Since the effort to develop methods to solve the *compressible* Euler equations has been intensive, there now exists a substantial assortment of computer software. This not only includes procedures for generating a wide variety of grids (Eriksson 1982) and for solving systems of first-order hyperbolic differential equations upon them (Rizzi & Eriksson 1984), but also others used to analyse the solution methods numerically (Eriksson & Rizzi 1983) and to display the computed results graphically. Practically all methods to solve the compressible Euler equations are based on the hyperbolic character of these equations. Unfortunately, if one tries to apply these methods to an *incompressible* flow in the limit of smaller and smaller Mach number, one finds that they do not work very satisfactorily. This is because the sound waves allowed in the mathematical model have a very high speed, and they dominate the system. If, however, only steady incompressible flow is of interest, the way around the difficulty is Chorin's artificial-compressibility concept (see Chorin 1967; Peyret & Taylor 1983).

In this concept an artificial time-dependent term is added to the continuity equation so that the governing equations become

$$\frac{1}{\rho_0}\frac{\partial p}{\partial t}+c^2 \operatorname{div} V=0, \quad \frac{\partial V}{\partial t}+(V\cdot\operatorname{grad})V+\frac{1}{\rho_0}\operatorname{grad} p=0,$$

where c is an arbitrary real parameter and ρ_0 is the constant density of the flow. This modified set of equations has no physical meaning until the steady state is reached. However, when this occurs the system becomes identical with the true steady equations. The still-arbitrary parameter c^2 can be selected to accelerate the time decay to steady state.

The major advantage of the modified system over the original one is that the high-speed sound waves have been eliminated, rendering the modified system much better conditioned for numerical solution. Note that the advantage here is very similar to the removal of gravity waves by the geostrophic approximation in the equations of meteorology. Surprisingly enough, Chorin's artificial-compressibility concept has attracted but a little attention, applications being primarily to the incompressible Navier–Stokes equations. The present application, it appears, is the first to the strictly inviscid incompressible equations.

Before describing an appropriate computational method, the mathematical character of the modified set of differential equations is investigated first.

2.2. *Hyperbolicity*

In three-dimensional Cartesian coordinates the conservation equations for the artificial-compressibility approach to steady incompressible flow are

$$\frac{\partial}{\partial t}\boldsymbol{q}+\boldsymbol{\theta}\cdot\left[\frac{\partial \boldsymbol{f}}{\partial x}+\frac{\partial \boldsymbol{g}}{\partial y}+\frac{\partial \boldsymbol{h}}{\partial z}\right]=0, \tag{1}$$

where

$$\boldsymbol{q}=\begin{bmatrix} p/\rho_0 \\ u \\ v \\ w \end{bmatrix}, \quad \boldsymbol{\theta}=\begin{bmatrix} c^2 & 0 & 0 & 0 \\ 0 & 1 & 0 & 0 \\ 0 & 0 & 1 & 0 \\ 0 & 0 & 0 & 1 \end{bmatrix},$$

$$\boldsymbol{f}=\begin{bmatrix} u \\ u^2+p/\rho_0 \\ uv \\ uw \end{bmatrix}, \quad \boldsymbol{g}=\begin{bmatrix} v \\ uv \\ v^2+p/\rho_0 \\ vw \end{bmatrix}, \quad \boldsymbol{h}=\begin{bmatrix} w \\ uw \\ vw \\ w^2+p/\rho_0 \end{bmatrix},$$

and c can be chosen to accelerate the time decay to steady state. The equivalent quasilinear form of system (1) is

$$\frac{\partial}{\partial t}\boldsymbol{q}+\boldsymbol{A}\frac{\partial}{\partial x}\boldsymbol{q}+\boldsymbol{B}\frac{\partial}{\partial y}\boldsymbol{q}+\boldsymbol{C}\frac{\partial}{\partial z}\boldsymbol{q}=0, \tag{2}$$

with

$$\boldsymbol{A}=\boldsymbol{\theta}\cdot\frac{\partial \boldsymbol{f}}{\partial \boldsymbol{q}}=\begin{bmatrix} 0 & c^2 & 0 & 0 \\ 1 & 2u & 0 & 0 \\ 0 & v & u & 0 \\ 0 & w & 0 & u \end{bmatrix}, \quad \boldsymbol{B}=\boldsymbol{\theta}\cdot\frac{\partial \boldsymbol{g}}{\partial \boldsymbol{q}}=\begin{bmatrix} 0 & 0 & c^2 & 0 \\ 0 & v & u & 0 \\ 1 & 0 & 2v & 0 \\ 0 & 0 & w & v \end{bmatrix},$$

$$\boldsymbol{C} = \boldsymbol{\theta}\cdot\frac{\partial \boldsymbol{h}}{\partial \boldsymbol{q}} = \begin{bmatrix} 0 & 0 & 0 & c^2 \\ 0 & w & 0 & u \\ 0 & 0 & w & v \\ 1 & 0 & 0 & 2w \end{bmatrix}.$$

It is called hyperbolic at the point $(x, y, z, t, \boldsymbol{q})$ if there exists a non-singular matrix $\boldsymbol{T}(\alpha, \beta, \epsilon)$ that diagonalizes the linear combination $\boldsymbol{D} = \alpha\boldsymbol{A} + \beta\boldsymbol{B} + \epsilon\boldsymbol{C}$,

$$\boldsymbol{T}^{-1}\boldsymbol{D}\boldsymbol{T} = \begin{bmatrix} \lambda^{(1)} & 0 & 0 & 0 \\ 0 & \lambda^{(2)} & 0 & 0 \\ 0 & 0 & \lambda^{(3)} & 0 \\ 0 & 0 & 0 & \lambda^{(4)} \end{bmatrix},$$

where the eigenvalues λ of $\boldsymbol{D}$ are real and the norms of $\boldsymbol{T}$ and $\boldsymbol{T}^{-1}$ are uniformly bounded for arbitrary real α, β and ϵ. The eigenvalues of $\boldsymbol{D}$ are found with the definitions $U = \alpha u + \beta v + \epsilon w$ and $a^2 = U^2 + c^2(\alpha^2 + \beta^2 + \epsilon^2)$, to be $\lambda^{(1)} = \lambda^{(2)} = U$, $\lambda^{(3)} = U + a$, $\lambda^{(4)} = U - a$, and are always real. Notice that the range between the smallest and largest eigenvalues can be adjusted according to the value of the parameter c. Using matrix $\boldsymbol{D}$'s complete set of linearly independent right eigenvectors as the columns of matrix $\boldsymbol{T}$, we find

$$\boldsymbol{T} = \begin{bmatrix} 0 & 0 & c^2 a & -c^2 a \\ -\epsilon & -\beta & u(U+a) + \alpha c^2 & u(U-a) + \alpha c^2 \\ 0 & \alpha & v(U+a) + \beta c^2 & v(U-a) + \beta c^2 \\ \alpha & 0 & w(U+a) + \epsilon c^2 & w(U-a) + \epsilon c^2 \end{bmatrix}. \tag{3}$$

Its inverse is formed from the left eigenvectors of $\boldsymbol{D}$:

$$\boldsymbol{T}^{-1} = \begin{bmatrix} \dfrac{\epsilon U - (\alpha^2+\beta^2+\epsilon^2) w}{\alpha a^2} & -\dfrac{wU + \epsilon c^2}{a^2} & -\dfrac{\beta(wU + \epsilon c^2)}{\alpha a^2} & \dfrac{(\alpha u + \beta v)\, U(\alpha^2+\beta^2) c^2}{\alpha a^2} \\ \dfrac{\beta U - (\alpha^2+\beta^2+\epsilon^2) v}{\alpha a^2} & -\dfrac{vU + \beta c^2}{a^2} & \dfrac{(\alpha u + \epsilon w)\, U + (\alpha^2+\epsilon^2) c^2}{\alpha a^2} & -\dfrac{\epsilon(vU + \beta c^2)}{\alpha a^2} \\ -\dfrac{U-a}{2a^2c^2} & \dfrac{\alpha}{2a^2} & \dfrac{\beta}{2a^2} & \dfrac{\epsilon}{2a^2} \\ -\dfrac{U+a}{2a^2c^2} & \dfrac{\alpha}{2a^2} & \dfrac{\beta}{2a^2} & \dfrac{\epsilon}{2a^2} \end{bmatrix} \tag{4}$$

Working with the maximum norm, one can then go on to complete the demonstration of hyperbolicity by making reasonable estimates to show that these last two matrices are uniformly bounded if $|u|$, $|v|$, and $|w|$ are bounded.

The equations that we actually solve, however, are not the Cartesian set (1) but the general finite-volume form (Rizzi & Eriksson 1984)

$$\frac{\partial}{\partial t}\int \boldsymbol{q}\, \mathrm{d}\,\mathrm{vol} + \boldsymbol{\theta}\cdot\iint \boldsymbol{H}\cdot\boldsymbol{n}\, \mathrm{d}s = 0, \tag{5}$$

where $\boldsymbol{H}\cdot\boldsymbol{n} = [\boldsymbol{V}\cdot\boldsymbol{n},\, u\boldsymbol{V}\cdot\boldsymbol{n} + (p/\rho_0)\boldsymbol{n}\cdot\boldsymbol{e}_x,\, v\boldsymbol{V}\cdot\boldsymbol{n} + (p/\rho_0)\boldsymbol{n}\cdot\boldsymbol{e}_y,\, w\boldsymbol{V}\cdot\boldsymbol{n} + (p/\rho_0)\boldsymbol{n}\cdot\boldsymbol{e}_z]$ is the vector flux of $\boldsymbol{q}$ across the surrounding grid of quadrilateral cells with volume VOL and vector areas $\boldsymbol{S}_I = SIX\boldsymbol{e}_x + SIY\boldsymbol{e}_y + SIZ\boldsymbol{e}_z$, $\boldsymbol{S}_J = SJX\boldsymbol{e}_x + SJY\boldsymbol{e}_y + SJZ\boldsymbol{e}_z$

and $\boldsymbol{S}_K = SKX\boldsymbol{e}_x + SKY\boldsymbol{e}_y + SKZ\boldsymbol{e}_z$. We can analyse (5) locally, after semidiscretization using centred space differences, by holding the metrics of the cell ijk constant to obtain

$$\frac{\mathrm{d}}{\mathrm{d}t}(\boldsymbol{q}\ \mathrm{vol})_{ijk} + (\bar{\boldsymbol{A}}\delta_I + \bar{\boldsymbol{B}}\delta_J + \bar{\boldsymbol{C}}\delta_K)\, q_{ijk} = 0, \tag{6}$$

where

$$\bar{\boldsymbol{A}} = \boldsymbol{\theta}\cdot\frac{\partial(\boldsymbol{H}\cdot\boldsymbol{S}_I)}{\partial\boldsymbol{q}} = \begin{bmatrix} 0 & c^2SIX & c^2SIY & c^2SIZ \\ SIX & U+uSIX & uSIY & uSIZ \\ SIY & vSIX & U+vSIY & vSIZ \\ SIZ & wSIX & wSIY & U+wSIZ \end{bmatrix},$$

$$\bar{\boldsymbol{B}} = \boldsymbol{\theta}\cdot\frac{\partial(\boldsymbol{H}\cdot\boldsymbol{S}_J)}{\partial\boldsymbol{q}} = \begin{bmatrix} 0 & c^2SJX & c^2SJY & c^2SJZ \\ SJX & V+uSJX & uSJY & uSJZ \\ SJY & vSJX & V+vSJY & vSJZ \\ SJZ & wSJX & wSJY & U+wSJZ \end{bmatrix},$$

$$\bar{\boldsymbol{C}} = \boldsymbol{\theta}\cdot\frac{\partial(\boldsymbol{H}\cdot\boldsymbol{S}_K)}{\partial\boldsymbol{q}} = \begin{bmatrix} 0 & c^2SKX & c^2SKY & c^2SKZ \\ SKX & W+uSKX & uSKY & uSKZ \\ SKY & vSKX & W+vSKY & vSKZ \\ SKZ & wSKX & wSKY & W+wSKZ \end{bmatrix},$$

with

$$U = uSIX + vSIY + wSIZ, \quad V = uSJX + vSJY + wSJZ,$$

and

$$W = uSKX + vSKY + wSKZ.$$

Since the three matrices $\bar{\boldsymbol{A}}$, $\bar{\boldsymbol{B}}$ and $\bar{\boldsymbol{C}}$ in (6) are linear combinations of $\boldsymbol{A}$, $\boldsymbol{B}$ and $\boldsymbol{C}$, (6) also is hyperbolic, and its eigenvalues and diagonalizing matrices follow from (3) and (4) by absorbing the metrics into α, β and ϵ.

2.3. *Value for parameter c*

Although the finite-volume transformation does not destroy the hyperbolicity of the problem, specifying an inappropriate value for the parameter c may degrade its condition if the different wave speeds in the system become too disparate. In order to guide us in choosing a value for c, we need to look at a measure more quantitative than just the boundedness of the transformation matrices. In fact what we want to know is how the bound varies with c. This can be determined numerically for given values of $\boldsymbol{V}$ and c by computing the eigenvalues σ of $\boldsymbol{T}^*\boldsymbol{T}$ since the L_2 norms are $\|\boldsymbol{T}\| = (\sigma_{\max})^{\frac{1}{2}}$ and $\|\boldsymbol{T}^{-1}\| = (\sigma_{\min})^{-\frac{1}{2}}$. It is less cumbersome, but sufficient for insight, to consider only the two-dimensional problem, i.e. $w = \epsilon = 0$. For any specified values of $\boldsymbol{V}$ and c a good measure of the condition of the system is the number $K = \|\boldsymbol{T}\|\,\|\boldsymbol{T}^{-1}\| = (\sigma_{\max}/\sigma_{\min})^{\frac{1}{2}}$. One can surmise, and we have verified it in an actual computation, that this condition number K depends only on the ratio $c^2/\boldsymbol{V}\cdot\boldsymbol{V}$. Computed numerically and plotted in figure 1 as the radial coordinate of the polar diagram (K, θ), where the wave angle θ defines $\alpha = \sin\theta$ and $\beta = \cos\theta$ for $0 \leqslant \theta \leqslant 2\pi$, the condition number K is displayed for three different values of $c^2/\boldsymbol{V}\cdot\boldsymbol{V}$. When the ratio $r = c^2/\boldsymbol{V}\cdot\boldsymbol{V}$ is greater than unity the pressure waves dominate over the convection waves and the system is less directionally dependent and better conditioned. This analysis applies to the constant-coefficient-matrix problem (6), but for

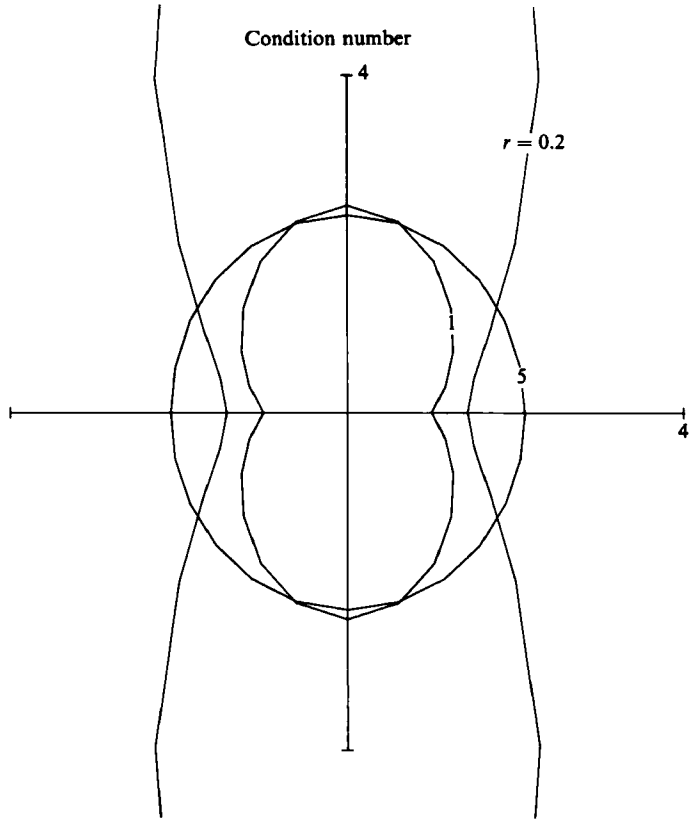

FIGURE 1. Polar diagram of condition number $K = \| \boldsymbol{T} \|_{L_2} \| \boldsymbol{T}^{-1} \|_{L_2}$ of the hyperbolic system (1) as a function of the plane wave angle θ for three values of the ratio $r = c^2/(u^2+v^2) = 0.2$, 1 and 5. Poorly conditioned when $r < 1$.

actually solving the flow field the parameter c need not be a global constant. In the spirit of local-timestep scaling (Rizzi & Eriksson 1984) we set it proportional to the local velocity squared, $c^2 = \max(0.3, r\boldsymbol{V}\cdot\boldsymbol{V})$ where, based on this study, r is a constant in the range $1 < r < 5$.

2.4. *CFL condition*

In order to solve the hyperbolic system (5), assuming that under appropriate boundary conditions it does converge to a steady state, we straightforwardly apply the time-marching finite-volume procedure developed originally for the compressible Euler equations which uses an explicit three-stage Runge–Kutta-type time-integration scheme (see Rizzi & Eriksson 1984). In the absence of boundaries the usual linearized Fourier analysis of (6) specifies the limit on the timestep for which the integration locally is stable, i.e. the *CFL* condition is $\Delta t \leqslant CFL/|\lambda|_{\max}$ where the constant *CFL* depends on the particular multistage method that is used. A conservative estimate for the maximum eigenvalue $|\lambda|_{\max}$ of the 3-dimensional spatial-difference operator leads to the local-timestep condition

$$\Delta t_{ijk} \leqslant CFL \left[\frac{\mathrm{VOL}}{\tilde{U} + (\tilde{U}^2 + c^2 S^2)^{\frac{1}{2}}} \right]_{ijk}, \tag{7}$$

where

$$\begin{aligned}\tilde{U} &= |uSIX+vSIY+wSIZ| \\ &\quad +|uSJX+vSJY+wSJZ| \\ &\quad +|uSKX+vSKY+wSKZ|, \\ S^2 &= (|SIX|+|SJX|+|SKX|)^2 \\ &\quad +(|SIY|+|SJY|+|SKY|)^2 \\ &\quad +(|SIZ|+|SJZ|+|SKZ|)^2.\end{aligned}$$

The computed results we present here have all been carried out using this step size in the local-timestep integration scheme.

2.5. *Discontinuities*

In steady flow the true incompressible equations admit of course only the tangential discontinuity with jump conditions $[p] = 0$ and $\boldsymbol{V}_1 \cdot \boldsymbol{n} = \boldsymbol{V}_2 \cdot \boldsymbol{n} = 0$. The artificial-compressibility method, however, approaches steady flow only asymptotically in time, so we must investigate what transient discontinuities are allowed in this pseudo-system of equations. This aspect of the method has been overlooked, it seems, by Chorin (1967) and Peyret & Taylor (1983). We follow the standard analysis of discontinuities for conservation laws, and shrink the integration region in (5) around the discontinuity surface to obtain, in the limit,

$$\left.\begin{aligned} s[p] &= c^2[V_n], \\ s[V_n] &= [V_n^2+p] = 2V_n^*[V_n]+[p], \\ s[V_t] &= [V_n\, V_t] = V_n^*[V_t]+V_t^*[V_n], \end{aligned}\right\} \tag{8}$$

where s is the speed of the discontinuity in the direction of its normal $\boldsymbol{n}$, the tangential direction $\boldsymbol{t}$ is parallel to the surface, the asterisk indicates the average of the values on each side of the discontinuity, e.g. $V_n^* = \frac{1}{2}(V_{n_1} + V_{n_2})$, and the square brackets their difference, $[V_n] = V_{n_2} - V_{n_1}$. System (8) is linear and homogeneous for given s and average velocities,

$$\begin{pmatrix} -s & c^2 & 0 \\ 1 & 2V_n^*-s & 0 \\ 0 & V_t^* & V_n^*-s \end{pmatrix} \begin{pmatrix} [p] \\ [V_n] \\ [V_t] \end{pmatrix} = 0, \tag{9}$$

and a non-trivial solution exists if

$$(s-V_n^*)(s^2-2sV_n^*-c^2) = 0.$$

The discontinuity therefore may move with any of three different speeds, $s_1 = V_n^*$, $s_2 = V_n^* + (V_n^{*2}+c^2)^{\frac{1}{2}}$, or $s_3 = V_n^* - (V_n^{*2}+c^2)^{\frac{1}{2}}$. The jump relations for the first speed then are eigenvectors of (8), which work out to be

$$\begin{pmatrix} [p] \\ [V_n] \\ [V_t] \end{pmatrix} = \kappa \begin{pmatrix} 0 \\ 0 \\ 1 \end{pmatrix}, \quad \text{with } s = V_{n_1} = V_{n_2} = V_n^*, \tag{10}$$

and κ is an arbitrary constant. We immediately recognize this solution as the unsteady tangential discontinuity that corresponds directly to the steady one. The

second and third eigenvectors associated with the speeds $s = s_2$ and $s = s_3$ respectively,

$$\begin{pmatrix} [p] \\ [V_n] \\ [V_t] \end{pmatrix} = \kappa \begin{pmatrix} c^2 \\ s \\ s V_t^* (V_n^{*2} + c^2)^{-\frac{1}{2}} \end{pmatrix}, \tag{11}$$

are more unexpected, since they allow jumps in both pressure and velocity across a discontinuity. With $s = s_2$ the shock travels downstream, and the pressure and normal velocity of a fluid particle passing through it rises or falls together depending on the sign of κ. With $s = s_3$ the shock moves upstream and the jumps in pressure and normal velocity take opposite signs. One of these solutions may be spurious in the sense that it violates some sort of entropy condition that a real flow should fulfil if it were just slightly compressible, but we shall not pursue this matter further here. Of the two the second seems more physical, and specifies vanishing jumps in the limit as c^2 goes to zero. In any case, we presume that a fluid particle travelling through either one undergoes an irreversible process that produces a rise (or fall) in its entropy function and a corresponding loss (or gain) in its total pressure. But such a discontinuity is not allowed to remain a part of any steady flow field.

2.6. *Boundary conditions*

Boundary conditions of course specify the particular problem, and two different types are of concern here: flow conditions on a solid wall and at the far-field boundary of the mesh. Since our mesh is aligned to the wall, for the first type we set the velocity flux through the wall to zero and determine the pressure p on it from the normal component of the incompressible momentum equation $\boldsymbol{V} \cdot (\boldsymbol{V} \cdot \mathrm{grad})\, \boldsymbol{n} = \boldsymbol{n} \cdot \mathrm{grad}\, p/\rho_0$, which is exactly analogous to the conditions used for compressible flow (Rizzi 1978). When it is differenced to formally first-order accuracy, the pressure on the surface is deduced from the interior values.

The far-field conditions are specified as a form of Engquist's hierarchical series of absorbing boundary conditions (see Engquist & Majda 1978). The First Approximation of this theory reads that setting conditions on the characteristic variables, instead of the flow variables $\boldsymbol{q}$, of the component of (6) normal to the boundary, is maximally dissipative and therefore absorbs more energy. Selecting α, β and ϵ as the components of the unit vector normal to the boundary means that the eigenvalues λ of $\boldsymbol{D}$ are the slopes in time of the characteristic surfaces in the direction normal to the boundary. The transformation matrices $\boldsymbol{T}^{-1}$ and $\boldsymbol{T}$ diagonalize this one-dimensional equation so that

$$\frac{\partial}{\partial t} \boldsymbol{\phi} + \boldsymbol{\Lambda} \frac{\partial}{\partial \eta} \boldsymbol{\phi} = 0, \quad \text{where } \boldsymbol{\phi} = \boldsymbol{T}^{-1} \boldsymbol{q}, \quad \boldsymbol{\Lambda} = \boldsymbol{T}^{-1} \boldsymbol{D}, \quad \boldsymbol{T} = \mathrm{diag}\{\lambda^{(1)}, \lambda^{(2)}, \lambda^{(3)}, \lambda^{(4)}\}.$$

The combination of boundary conditions determined from outside the domain and auxiliary conditions set from inside follows in the now-standard way according to whether the associated characteristic directions enter or leave the domain. When $U < 0$ we set the three (corresponding to negative eigenvalues) ingoing characteristic variables $\phi^{(1)}$, $\phi^{(2)}$, and $\phi^{(4)}$ to their free-stream values, linearly extrapolate the third $\phi^{(3)}$ from the computational field, and then solve for the original unknowns $\boldsymbol{q} = \boldsymbol{T}\boldsymbol{\phi}$. At outflow it is $\phi^{(4)}$ that is given the values of undisturbed flow, and $\phi^{(1)}$, $\phi^{(2)}$ and $\phi^{(3)}$ are extrapolated.

2.7. *Artificial-viscosity model*

The rationale for introducing an artificial-viscosity operator into the numerical procedure has been put forward before (Eriksson & Rizzi 1984). Among the reasons to consider such a model are the need to counteract nonlinear aliasing associated with centred differences, to control the cascading of energy from large scale to small scale, and perhaps even to ensure the existence of a steady state. The dissipative operator $\boldsymbol{Dq}$ that we add to the convective differencing of the incompressible Euler equations contains a linear fourth-difference term for each of the three spatial directions (see Rizzi & Eriksson 1984). They are implemented with boundary conditions so that the complete operator has the negative semi-definite property $(\boldsymbol{q}^{\mathrm{T}}\boldsymbol{Dq}) \leqslant 0$, which has been found important for minimizing the occurrence of spurious errors at solid boundaries (see Eriksson 1984).

3. Computed results

Irrotational incompressible flow is governed by the Laplace equation, a linear equation. Laplace solutions also satisfy the nonlinear incompressible Euler equations, since then the term $\boldsymbol{V} \times \operatorname{curl} \boldsymbol{V}$ is zero, but other, nonlinear roots are admissible also. Why or in what way during the course of the numerical solution of this nonlinear system does the computational method arrive at either the Laplace solution or the rotational one we cannot answer conclusively right now. Certainly the boundary conditions, the initial conditions (whether they contain discontinuities or not), the geometry of obstacles to the flow, flow-field singularities, and the overall accuracy of the numerical method all have a central bearing on the question. In addition to demonstrating the overall soundness of the numerical method and outlining interesting flow features of a three-dimensional flow field, what we attempt to do with the computed results presented here is to show examples of both irrotational and rotational solutions and offer some plausible explanations why each was obtained.

3.1. *2-dimensional irrotational solution*

Our first example is inviscid incompressible flow past a circle, for which the analytical solution is known. Its comparison in figure 2 with the C_p pressure distribution computed by this method on the upper half-circle shows that indeed we do obtain the irrotational solution. The C_p distribution and the vector diagram of velocity directions (figure 3) indicate the fore-and-aft symmetry of the overall flow field and the loss-free character of the solution. However, if the numerical integration errors were larger than they actually are in this case, a loss in total pressure would occur, and the flow would stagnate and then separate before reaching the point most downstream on the circle. A recirculation region would subsequently develop in order to satisfy continuity, and rotational flow would result. In other words, a certain level of numerical accuracy is needed in order to obtain the irrotational solution; or, to put it another way, the amount of numerical viscosity must be kept to a minimum.

3.2. *2-dimensional solution with circulation*

The next example is also two-dimensional, but the entire plane is included now and the geometry is the NACA 0012 airfoil at 5° incidence. Measured by the decay of the average and maximum time difference of pressure in the entire field and the evolution of lift and drag, the convergence of the solution computed upon a mesh with 128 cells around the airfoil and 28 outward is given in figure 4. Although the comparison of

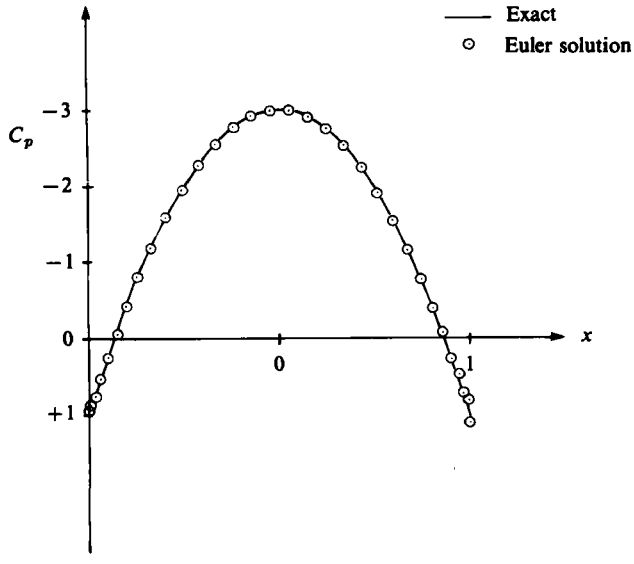

FIGURE 2. Comparison of the exact solution to the Laplace equation and the numerical solution to the Euler equations for incompressible flow around a circle.

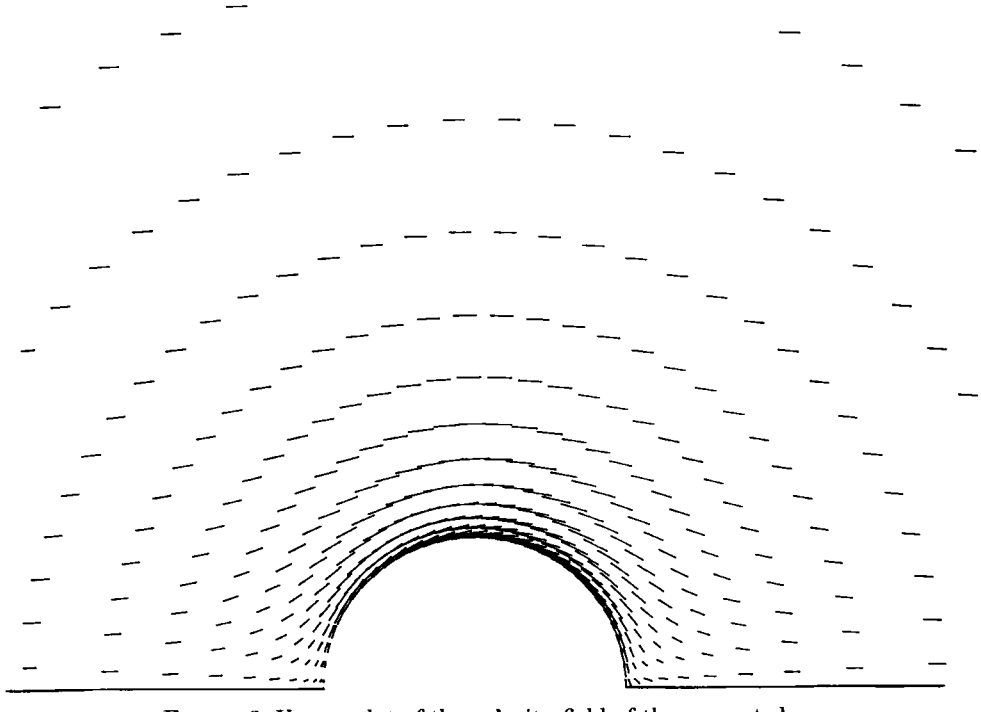

FIGURE 3. Vector plot of the velocity field of the computed Euler-equation solution to flow around the circle.

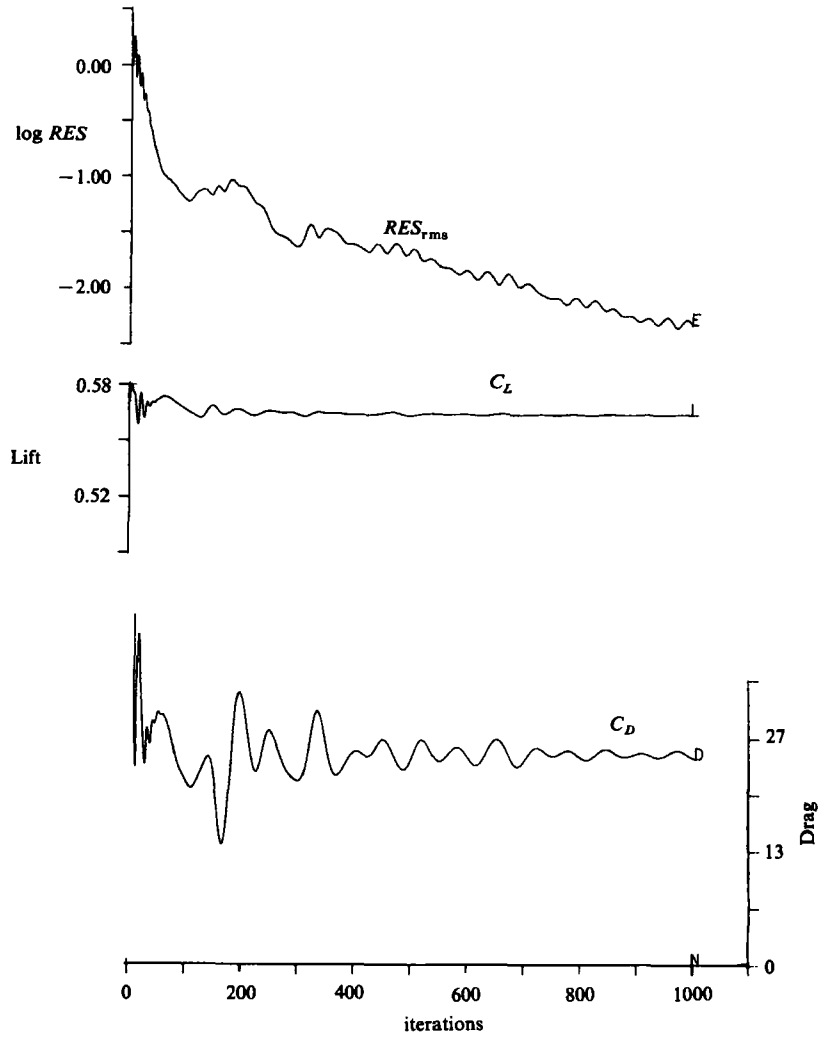

FIGURE 4. Convergence of the solution of incompressible flow past the NACA 0012 airfoil indicated by the decay of the average time difference of pressure and the evolution of lift and drag. $M_\infty = 0$, $\alpha = 5°$.

computed C_p on the airfoil with that of an accurate boundary-integral ('singularity', or so-called 'panel') method (Eriksson 1975) is generally good (figure 5), there are small discrepancies at the leading-edge suction peak and larger ones at the trailing edge, the latter due undoubtedly in part to the mesh being unable to resolve the flow singularity completely there. But perhaps the best gauge of accuracy is the degree to which the Bernoulli relation along a streamline in steady flow, $p/\rho_0 + \frac{1}{2}V^2 = p_t$(constant), is satisfied. In this flow all streamlines originate from a constant free stream, so the total pressure p_t takes the same value on every streamline. The total-pressure coefficient $(p_t - p_\infty)/(p_{t\infty} - p_\infty)$ in figure 6 confirms that there are errors in the vicinity of the leading and trailing edges, but they are small in magnitude and confined locally to these two regions. This loss, however, should not be interpreted as a physical quantity that is transported along streamlines, but rather as an error perturbation upon the solution where the flow gradients are

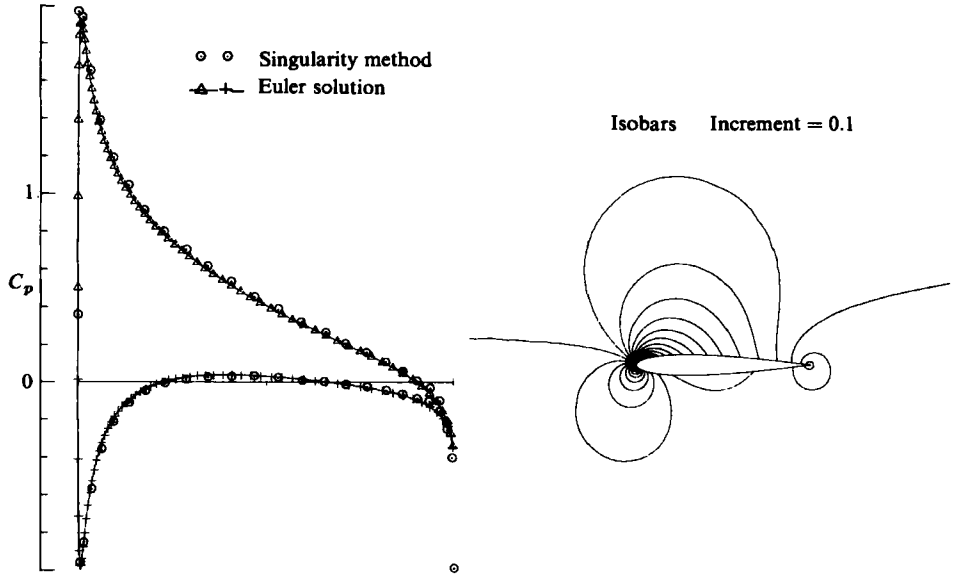

FIGURE 5. The pressure field of the computed Euler-equation solution. The surface distribution is compared with the highly accurate results from a potential singularity method. NACA 0012 airfoil, $M_\infty = 0$, $\alpha = 5°$.

especially large, which may be a possible source for the injection of vorticity. In regions where the flow gradients are not severe, an accurate value for the Bernoulli constant is produced. We conclude that an almost-irrotational solution is obtained with very nearly the correct circulation (as given by the panel method). Furthermore, the contours of constant flow angle (figure 7) demonstrate that even without our invoking a Kutta condition the flow leaves the trailing edge smoothly, which is an essential feature of potential flow showing a realistic amount of lift. The central question before us is therefore 'how does the Euler-equation method arrive at the correct circulatory flow?' (i.e. flow separation at the trailing edge without applying a Kutta condition). Although no definitive answer is yet at hand, some clues suggest that transient phenomena during the flow fields' evolution to steady state may be the significant agent. Figure 8 gives the values of lift C_L and circulation $\Gamma = \int \boldsymbol{V} \cdot \mathrm{d}\boldsymbol{l}$ around a circuit close to the airfoil obtained in the solution on each of its first 25 timesteps after starting from initial conditions of free-stream flow that do not satisfy the boundary conditions on the airfoil. We see that a non-zero value for lift is reached even after the first iteration. The circulation, however, tends to lag behind the lift, and in fact is even negative, suggesting, perhaps, the passage of vorticity opposite in sign to that bound in the airfoil. This observation follows the qualitative trend of the so-called Wagner effect (Wagner 1925). But the reader is cautioned against looking for quantitative realism in the transient field, because of the method's underlying assumption of artificial compressibility and its low order of accuracy for the time integration. At best, the broad features of the transient numerical solution may bear some similarity to the real physical processes. When we look in figure 9 at the contour maps of pressure and vorticity $\Omega = \boldsymbol{e}_z \cdot \mathrm{curl}\, \boldsymbol{V}$ of these solutions, we see a sharp pressure gradient moving out from the nose of the airfoil and another in the shadow of the trailing edge leaving behind them a high-pressure region of rotational flow. The vorticity distribution on the airfoil surface has peaks at the

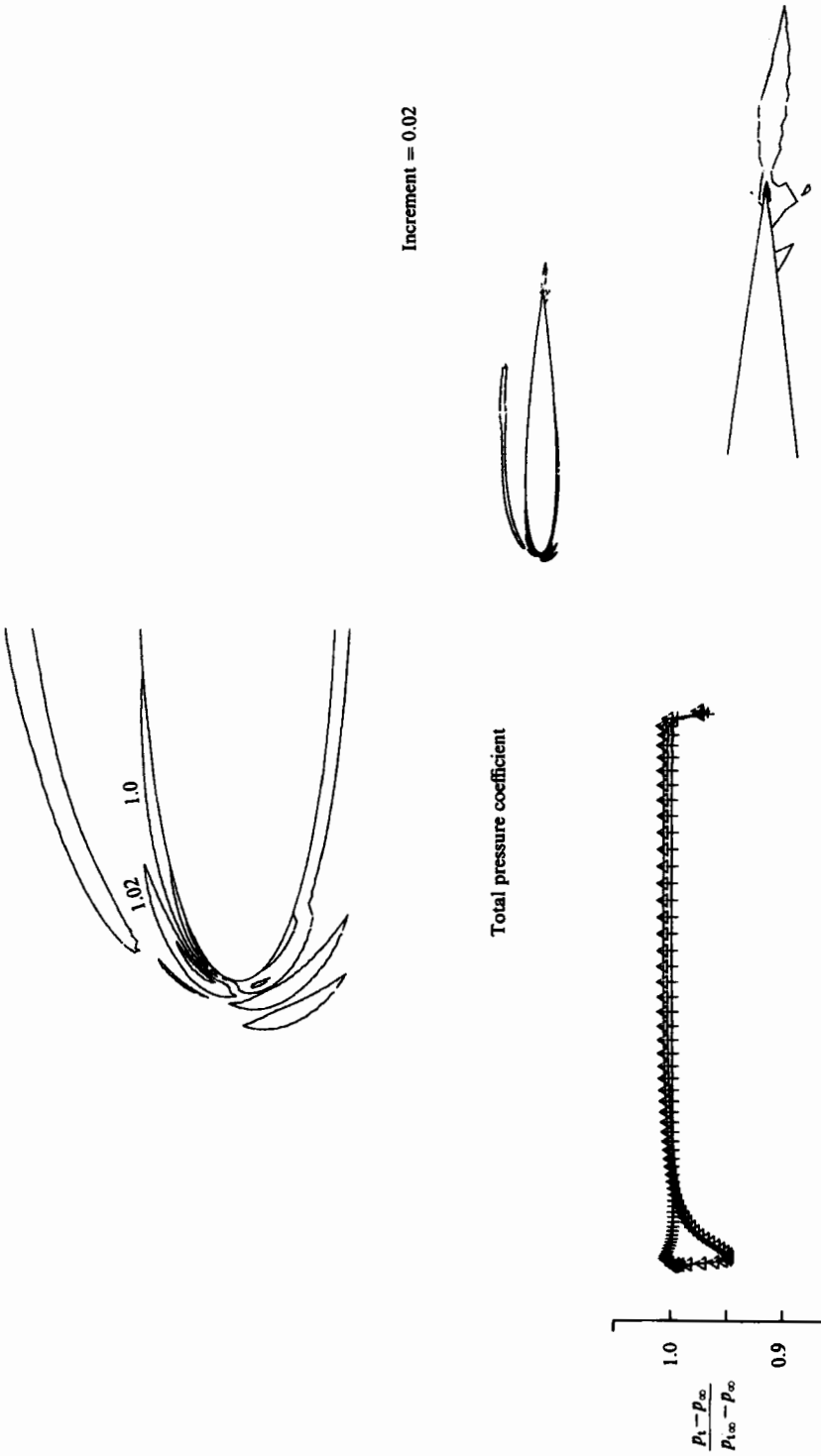

FIGURE 6. Accuracy of the computed Euler-equation solution indicated by total-pressure coefficient $(p_t - p_\infty)/(p_{t\infty} - p_\infty)$. NACA 0012 airfoil, $M = 0$, $\alpha = 5°$.

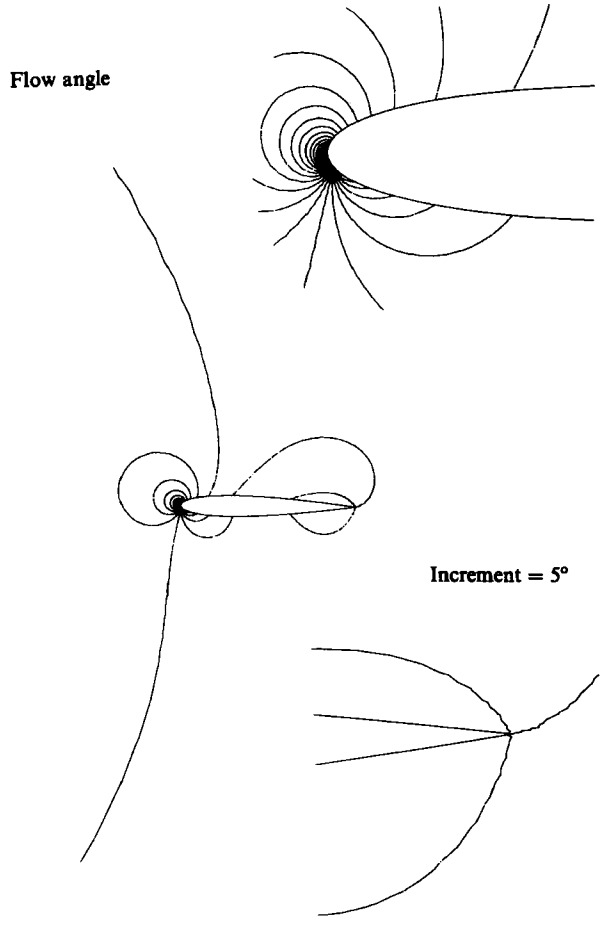

FIGURE 7. Contours of constant flow angle in the computed solution demonstrate that the flow leaves the trailing edge smoothly. NACA 0012, $M_\infty = 0$, $\alpha = 5°$.

leading and trailing edges, which achieve a maximum on the fifth iteration but then decay to the small residual level in the converged state by being swept out of the flow field. Presumably the vorticity created in the field is counterbalanced by a vortex bound in the airfoil which accounts for the circulation. But what causes the vorticity to appear in the first place? It is present in neither the freestream nor the initial conditions, and therefore seems to violate Kelvin's theorem. One possible explanation is that the large pressure waves ahead of the leading edge form the numerical approximation of one of the unsteady pseudoshock waves allowed in the artificial-compressibility method, and is the source of the vorticity. This source may be in part physical, the pseudoshock, and in part numerical, the viscosity of the discretization error. Substantial transient shear exists at the trailing edge and is swept downstream. It may well be the numerically smeared representation of an unsteady tangential discontinuity. We therefore hypothesize that the genesis of the circulation lies in irreversible processes, either in the mathematics itself or its numerical approximation, that occur across the transient pressure waves of the artificial-compressibility method. Once generated, the part that this vorticity plays, no matter how unphysical it may be, is to usher the iterative solution toward the rotational root of the

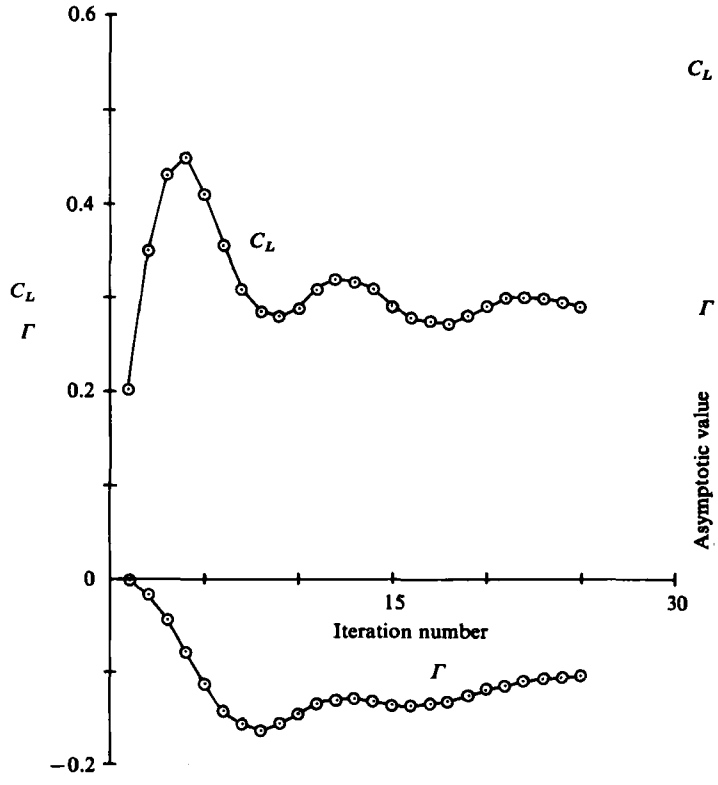

FIGURE 8. Evolution of lift and circulation during the first 25 iterations after an impulsive start from free-stream initial conditions. NACA 0012, $M_\infty = 0$, $\alpha = 5°$.

incompressible Euler equations. The trailing edge is evidently the controlling factor, namely the severe gradients subside only when the flow leaves the trailing edge smoothly.

3.3. *3-dimensional rotational solution*

This subsection presents the computed solution of incompressible flow around a 70° swept delta wing of zero thickness and unit length at 20° angle of attack. The steady flow separates from the leading edge in a vortex sheet, which then, under the influence of its own vorticity, rolls up to form a vortex over the wing. Owing to the lack of experimentally measured turbulent-flow data for this case, a comparison with measurements is not carried out. But we do compare our results with those from Hoeijmakers's potential boundary-integral (panel) method, which inserts a vortex sheet, adjusts it to the surrounding irrotational flow field, and allows it to roll up under its own influence for several turns, and then models the remaining core by an isolated line vortex (see Hoeijmakers, Vaatstra & Verhaagen 1983; Hoeijmakers & Rizzi 1984). The position and strength of the vortex sheet and isolated vortex are determined as part of the solution, sometimes termed 'fitting' the rotational-flow features. They are true discontinuities, infinitesimally thin, and for this reason a very good choice for comparison because the sheet and vortex in our solution are not infinitesimally thin but smeared or 'captured' over a number of computational mesh cells. The comparison therefore offers a good control on the position of our computed

(a)

FIGURE 9(a). For description see p. 296.

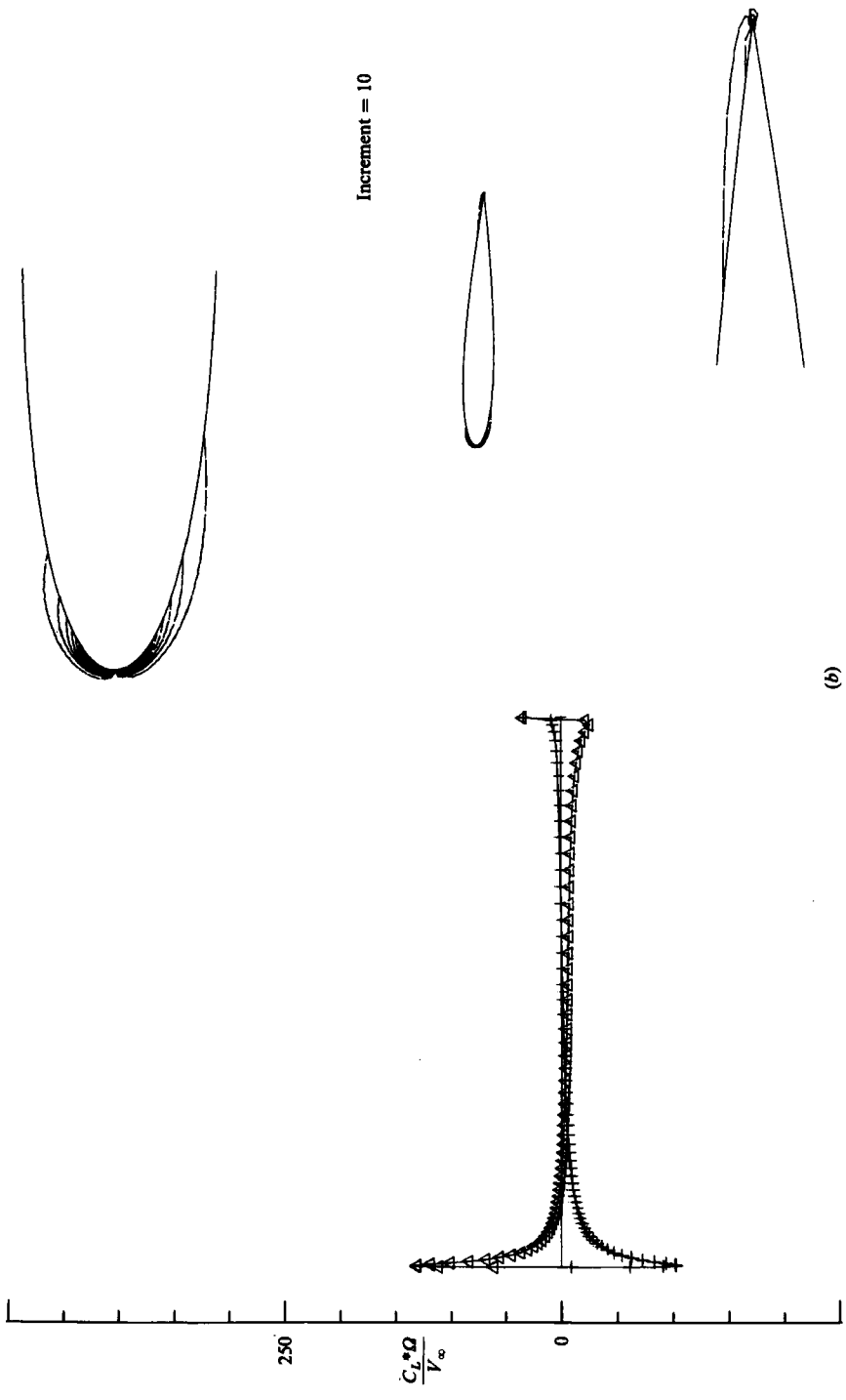

(*b*)

FIGURE 9 (*b*). For description see p. 296.

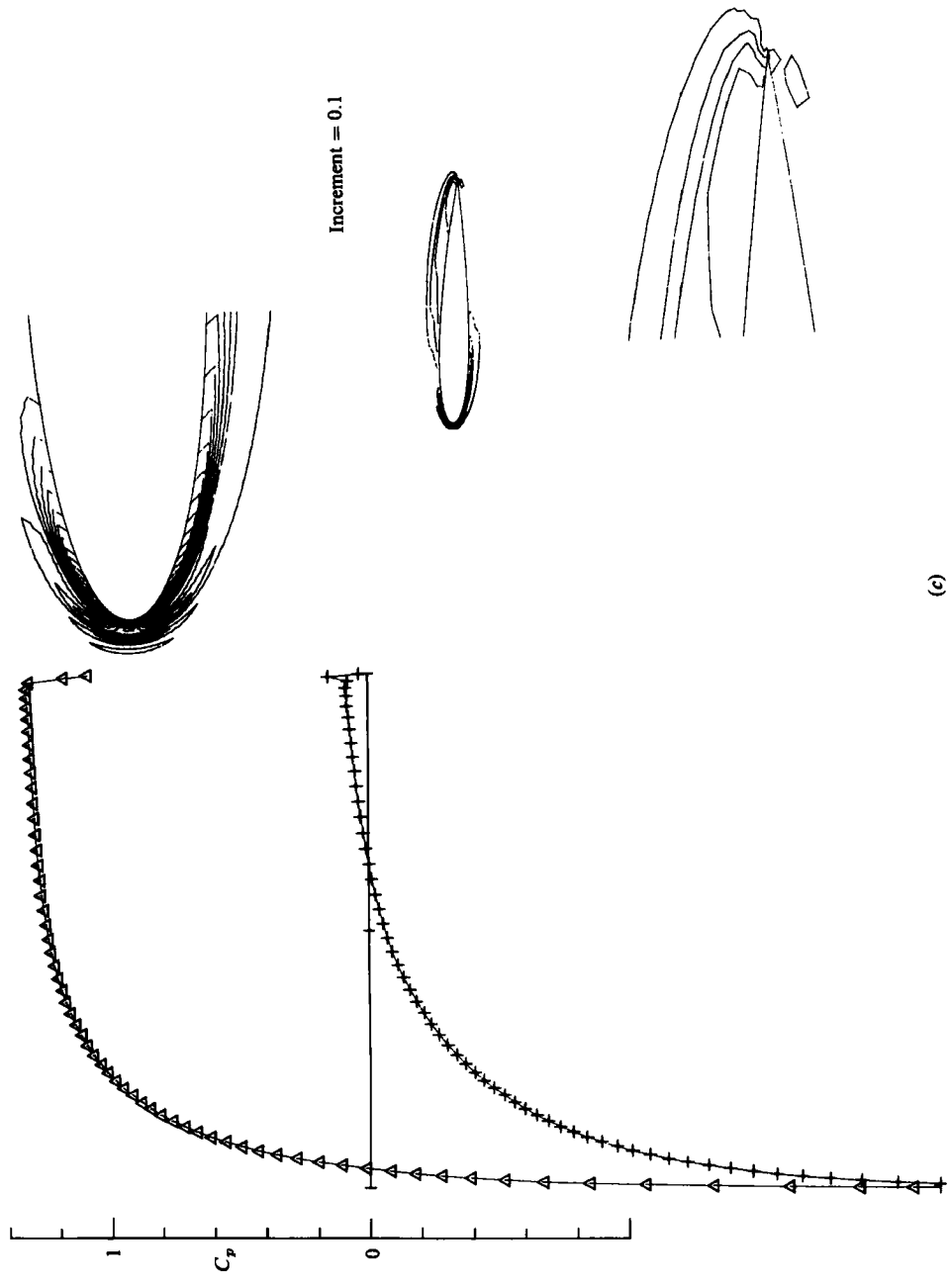

(c)

FIGURE 9(c). For description see p. 296.

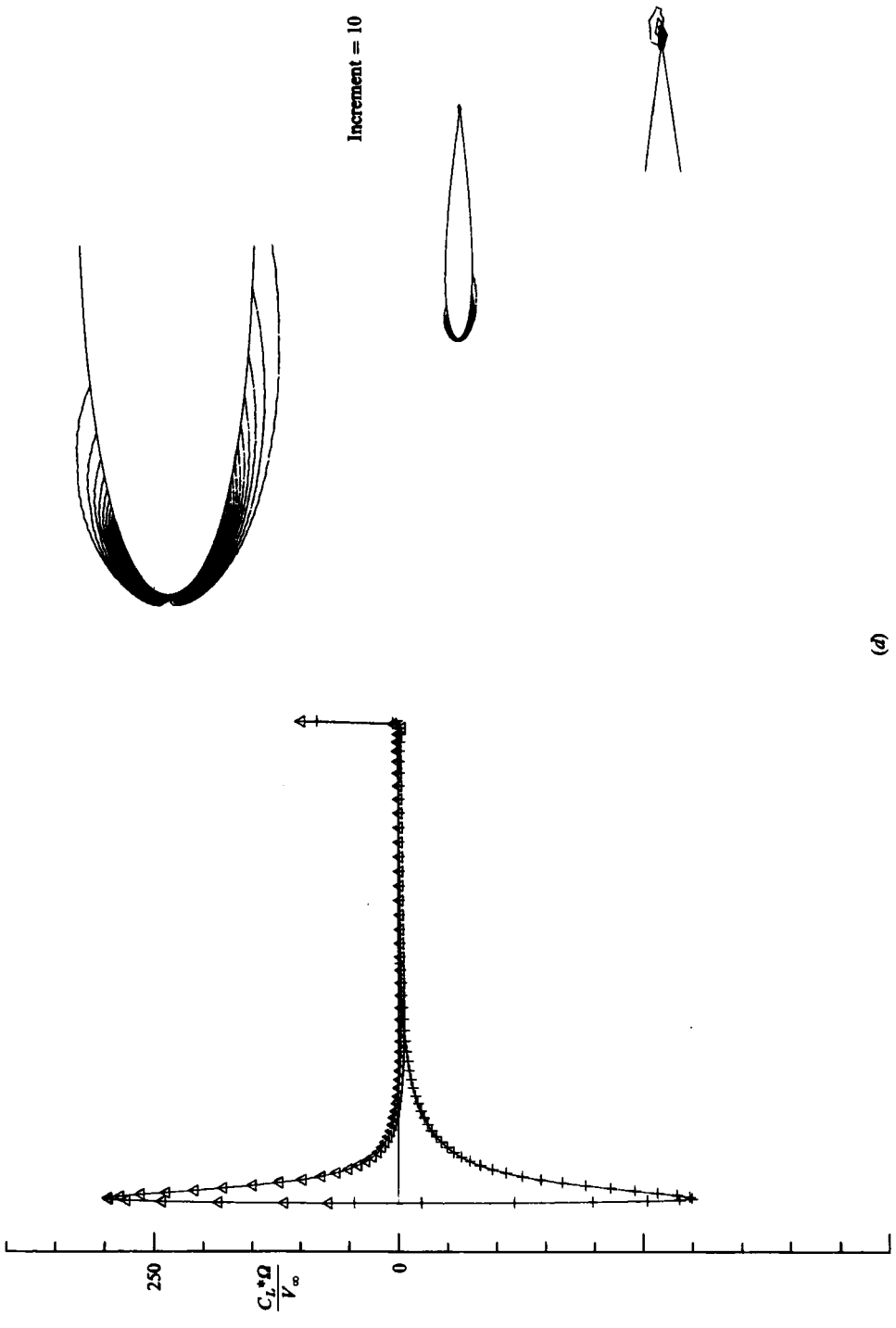

(*d*)

FIGURE 9(*d*). For description see p. 296.

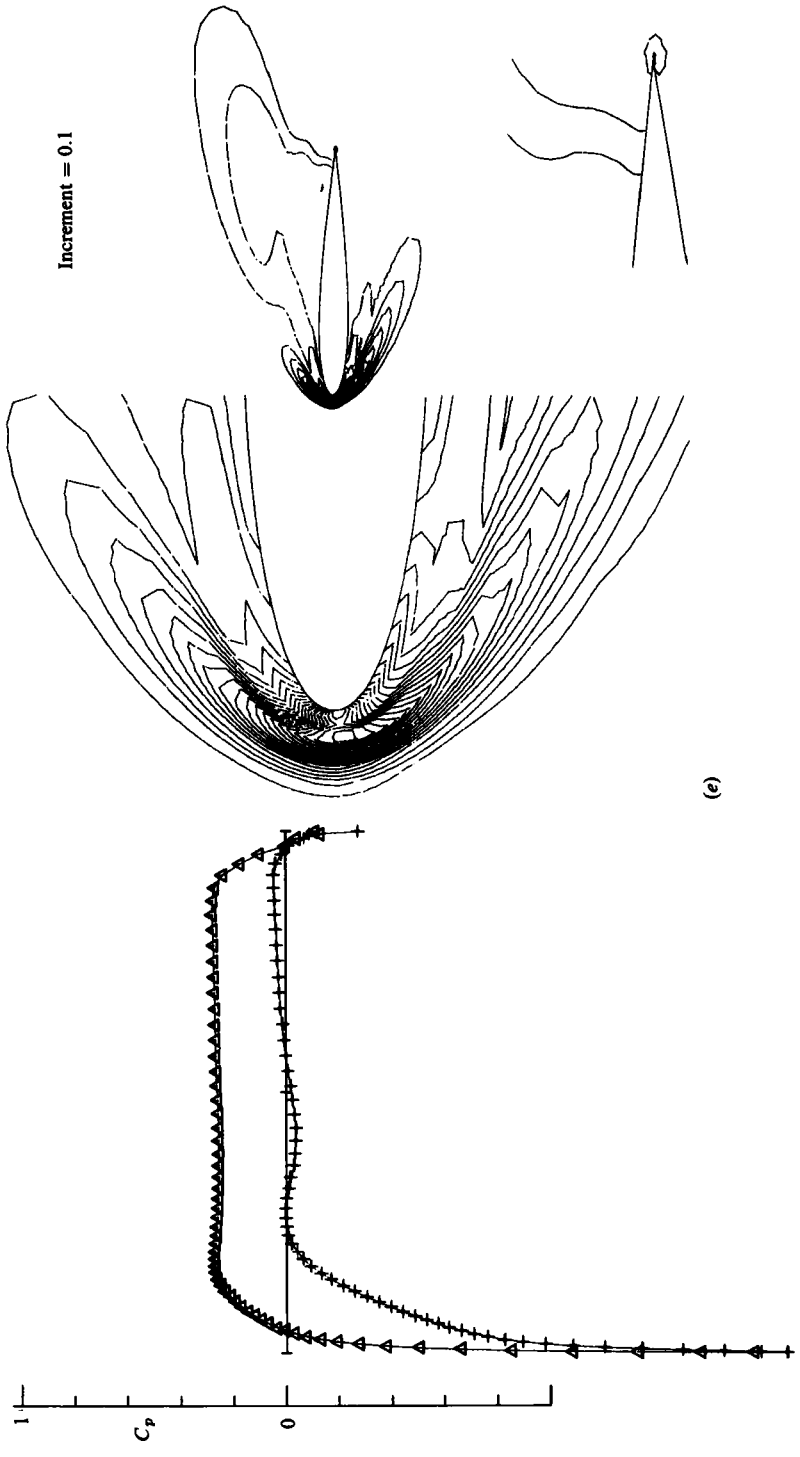

FIGURE 9(e). For description see p. 296.

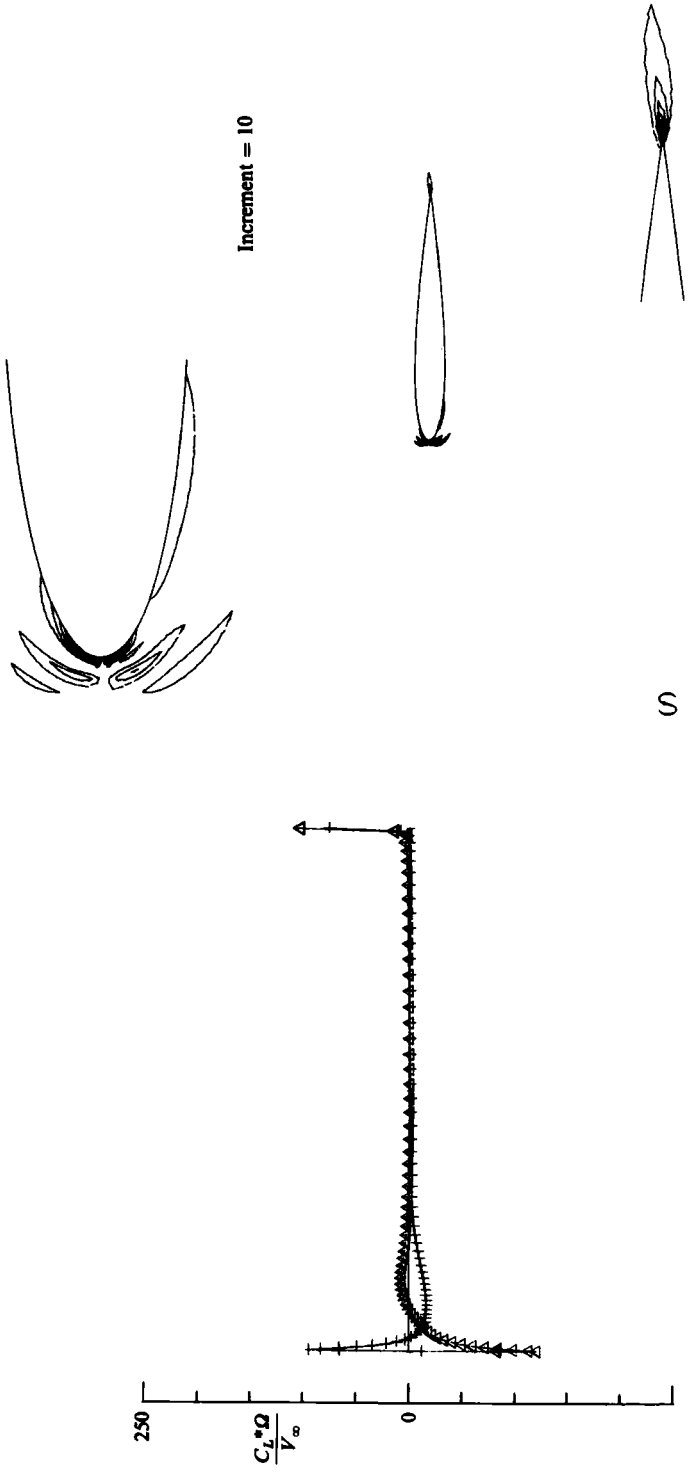

FIGURE 9(*f*). For description see p. 296.

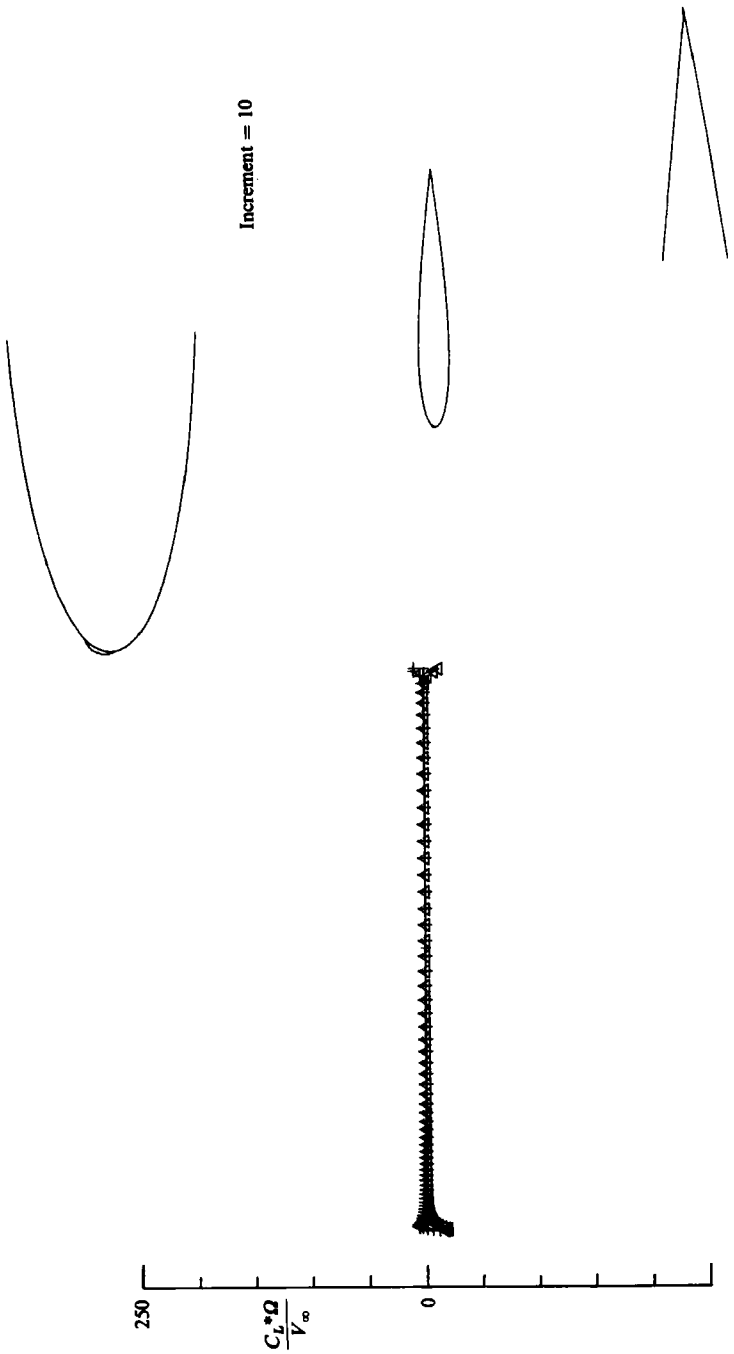

(g)

FIGURE 9. Contour maps of the pressure and vorticity fields during those early iterations. NACA 0012, $M_\infty = 0$, $\alpha = 5°$. (*a*) Pressure-field iteration; (*b*) vorticity-field iteration 1; (*c*) pressure-field iteration 5; (*d*) vorticity-field iteration 5; (*e*) pressure-field iteration 25; (*f*) vorticity-field iteration 25; (*g*) converged vorticity field.

vortex and the diffusion of the sheet. Furthermore such panel-method results have been found to agree reasonably well with measurements made in turbulent flow (see Hoeijmakers *et al.* 1983).

The thickness of the rotational flow features captured in the solution to the Euler equations varies directly with the size of the mesh cells. The simplest way, therefore, to minimize the diffusion of vorticity is to use as dense a mesh as possible. Ours is an 0–0 type constructed by Eriksson's (1982) interpolation method that places a polar singular line at the apex and a parabolic singular line at the tip of the trailing edge and has 80 cells around the half-span, 40 each on the upper and lower chord, and 24 outwards, for a total of 76800 cells (figure 10). This particular grid topology focuses cells along the leading and trailing edges, as well as the apex where the flow changes most rapidly. It requires, however, a slight rounding of the wingtip. Figure 11 presents a summary of the time evolution of the solution given by the root-mean-square and maximum residuals of the time difference of p, and by the lift and drag coefficients. After 800 timesteps taking 400 CP seconds, a steady state was reached, as judged by the decay of the residuals by several orders of magnitude. The computation was carried out on the CYBER 205 vector computer in 32-bit precision at the rate of 6 μs per cell per iteration, which translates to over 125 mflops.

Global features of the flow are surveyed in figure 12 by isograms, drawn in plane projection, of the computed solution in three non-planar mesh surfaces, $x/c = 0.3$, 0.6 and 0.9, over the wing, one surface in the wake at $x/c = 1.15$ and one cutting axially through the core of the vortex. The isograms of C_p, vorticity magnitude $|\boldsymbol{\Omega}|$, and total-pressure coefficient $(p_t - p_\infty)/(p_{t\infty} - p_\infty)$ in figures 12(*a–c*) reveal qualitatively the leading-edge vortex over the wing, as well as the trailing-edge vortex that develops from the trailing-edge sheet, interacts, and counter-rotates with the leading-edge vortex, and produces the double-vortex pattern in the wake. This wake phenomenon has been observed in a wind tunnel (Hummel 1979). The axial velocity component u/V_∞ is discontinuous across the sheet, and the contours in figure 12(*d*) clearly reveal this feature and also show that the velocity in the core is about 1.5 times the free-stream value. Contours of the circumferential velocity component $(v^2 + w^2)^{\frac{1}{2}}/V_\infty$ indicate the large gradients in this quantity across the core of the vortex. The isograms viewed axially through the core indicate the approximately conical nature of the flow starting at the apex. At about the 80% chord position, however, the leading-edge vortex lifts up slightly, and an abrupt change takes place which might be interpreted as an additional, and unexpected, vortex phenomenon. Although the cause of this feature may be numerical, it is known that the shear layer separating from the leading edge does show small-scale wave-like structure near the trailing edge (Hoeijmakers & Vaatstra 1983), which could perhaps evolve into a second vortex that wraps up and intertwines with the primary vortex (Hoeijmakers, private communication). It may also be a precursory effect of the development of the trailing-edge vortex. If the conjecture of such a flow process is correct, then our rounding of the tip just exacerbates it. The contours of total pressure (figure 12*c*) display qualitative agreement with those observed in wind-tunnel measurements. The computed losses in the core, however, are high, nearly 80% of the total pressure, and can be attributed to the numerical effect of capturing the vortex sheet. Theoretically the loss should be zero (total pressure coefficient = 1) on each side of the sheet, but the velocity is in shear. The numerical solution has to support this shear with a continuous profile over several mesh cells through the sheet, and any sort of reasonable profile (say a linear one) connecting the velocity vector on one side with the one on the other side immediately implies a total-pressure loss for the profile even if the velocities at both

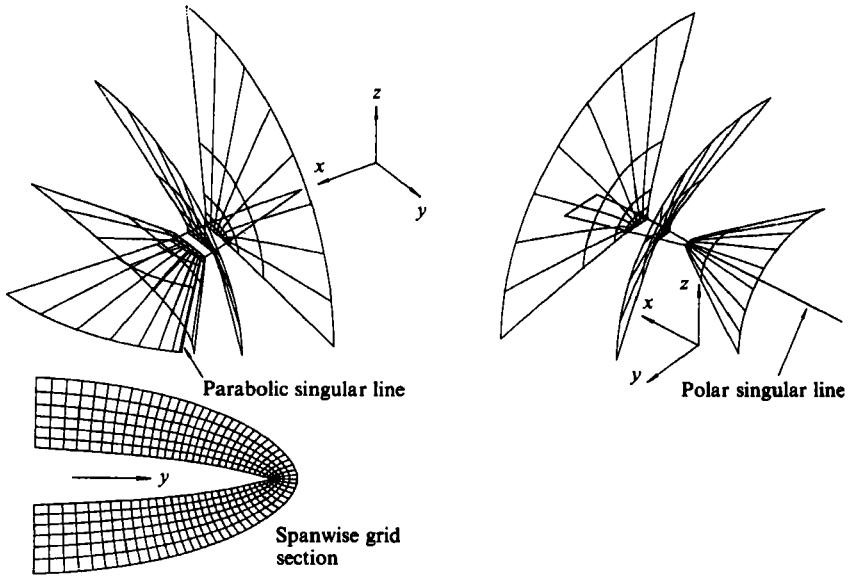

(a)

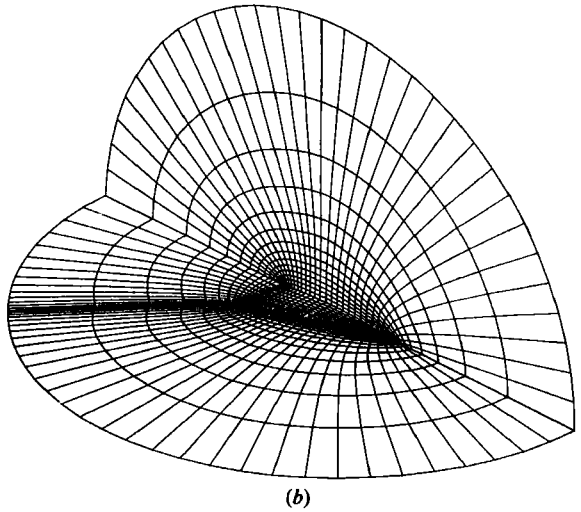

(b)

FIGURE 10(a) and (b). For description see opposite.

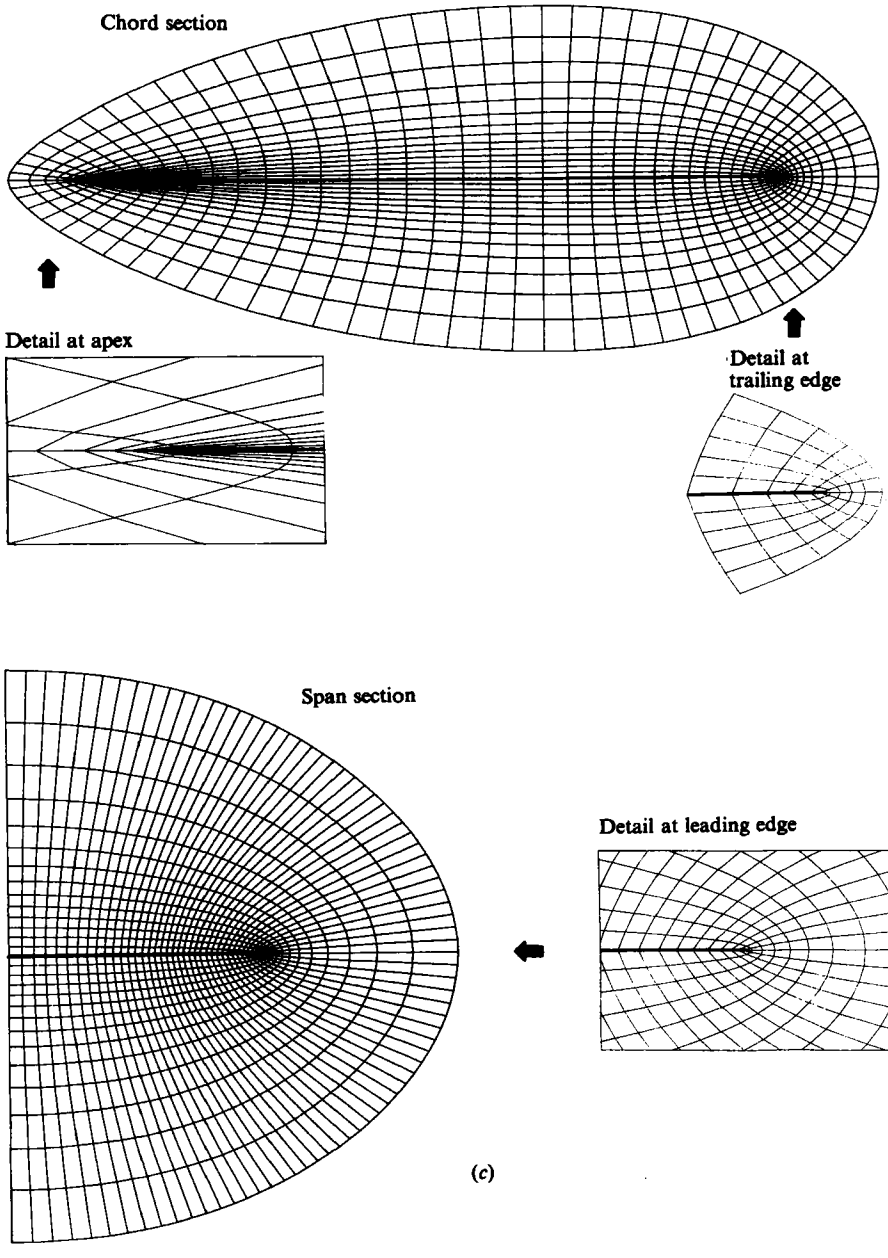

FIGURE 10. (*a*) Main features of an 0–0 grid generated around a delta-shaped small-aspect-ratio wing. The polar singular line produces a dense and nearly conical distribution of points at the apex, which is needed to resolve the rapidly varying flow there. (*b*) Three-dimensional view of the delta-wing mesh. (*c*) Partial chordwise and spanwise views of the actual $80 \times 24 \times 40$ mesh used for the computation of the 70° swept flat plate.

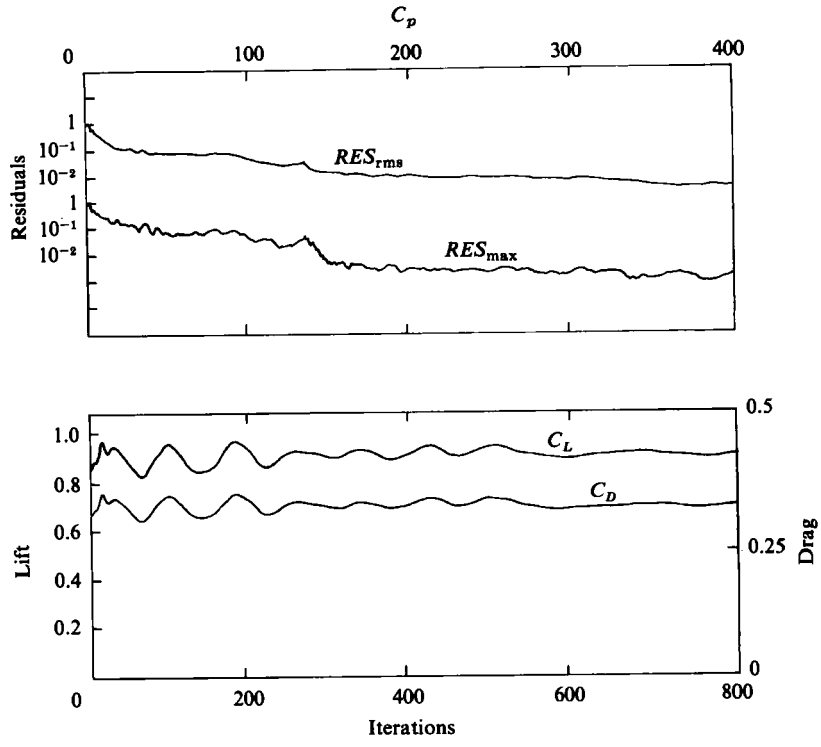

FIGURE 11. Convergence of the 3-dimensional Euler-equation solution for flow separating from the leading edge of a swept flat-plate delta wing indicated by the residual decay and evolution of lift and drag. $M = 0$, $\alpha = 20°$. CYBER 205 vector computer.

sides are correct. And the level of loss quickly mounts as the number of cells available to support the profile diminishes. As the vortex sheet wraps up tighter and tighter there will be only one or two cells located between the coils, and ultimately it will disappear off the mesh completely. At that point it is not unreasonable to expect the amount of loss of total pressure that we see in figure 12 (*c*). A finer mesh could support more coils, but the sheet must eventually disappear in the same way off this mesh too, producing about the same loss at the centre of a now smaller-diameter core. It is the size of the contour rings, but not their level, that varies with mesh spacing.

Let us now inspect the solution more quantitatively by comparison with the results of the potential method. Figure 13 presents the shape of the fitted vortex sheet (dashed lines) from the potential method superimposed upon the vorticity magnitude contours of the Euler-equation solution in three cross-flow planes. We should bear in mind that the dashed lines are in the planes x/c = constant, while the full lines are projections onto these planes of the vorticity contours in the non-planar mesh surfaces that intersect the wing at the corresponding value of x/c. We see that the vorticity captured in the field is diffused over 5 or 6 cells and that, in general, the vortical flow region occupies a larger volume than that enclosed by the vortex sheet fitted to the potential solution. But the positions of the vortex cores in the two results and even the curvature of the sheets agree remarkably well, except at the first station $x/c = 0.3$, where the vorticity contours are somewhat larger and more inboard of the fitted vortex sheet. The vorticity in the fitted sheet is largest near the leading edge, where the curvature of the sheet is greatest, perhaps even singular, and the

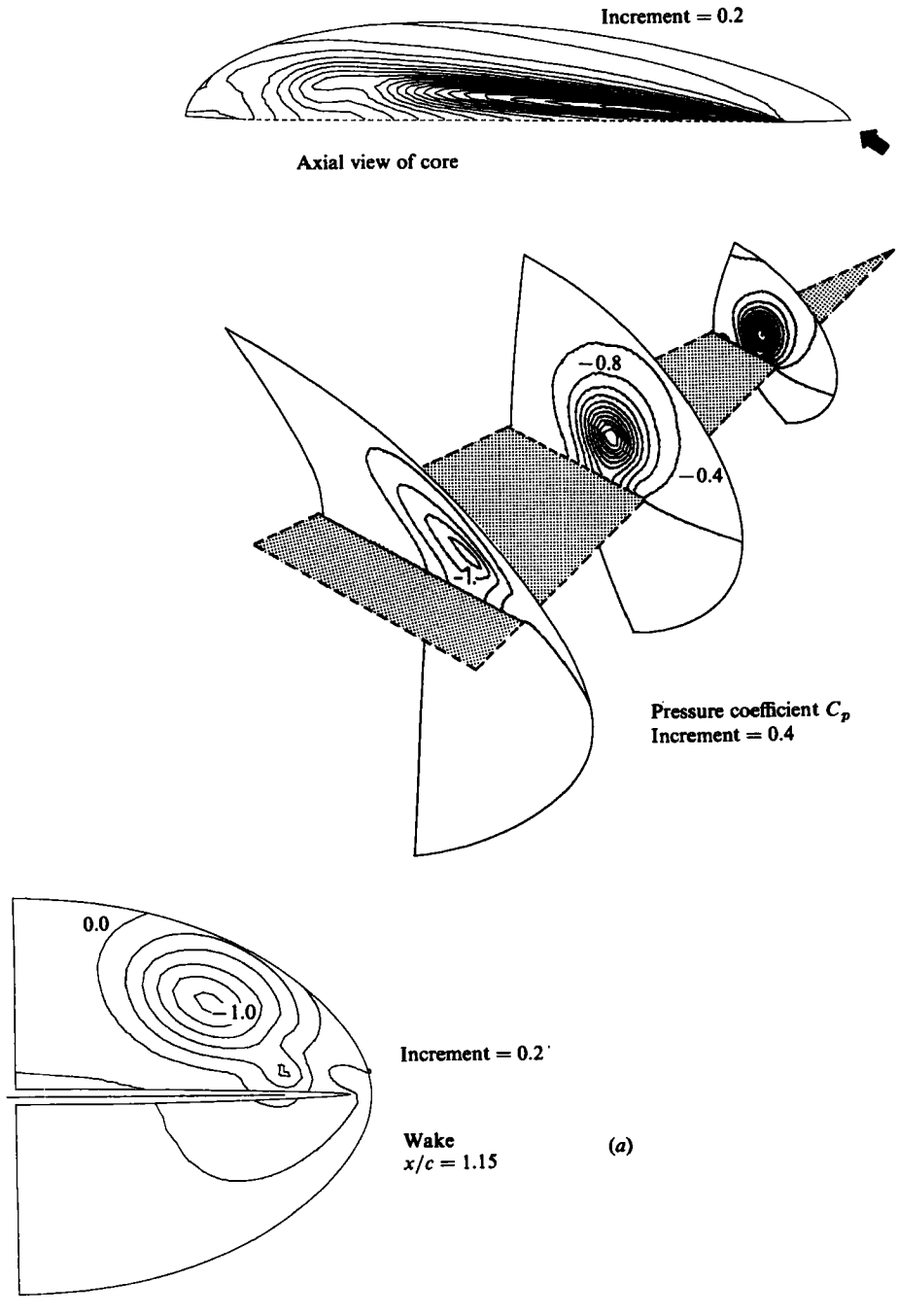

FIGURE 12(*a*). For description see p. 305.

Axial view of core

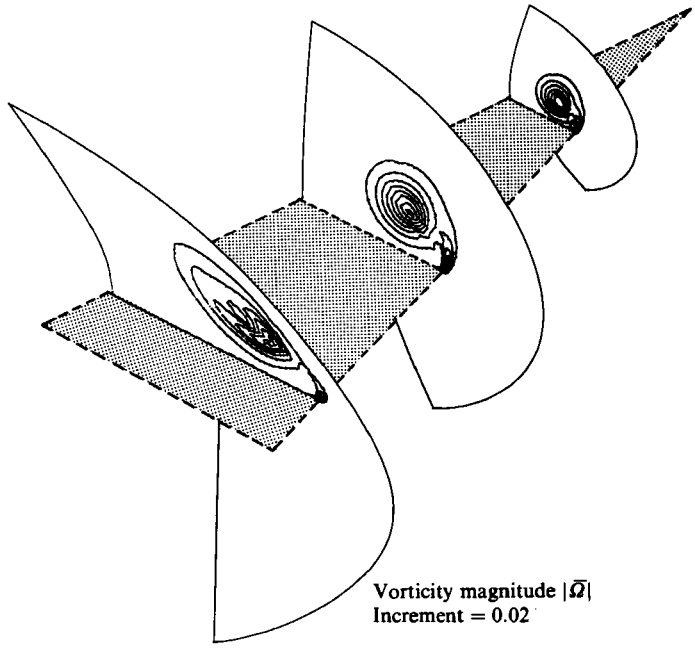

Vorticity magnitude $|\bar{\Omega}|$
Increment = 0.02

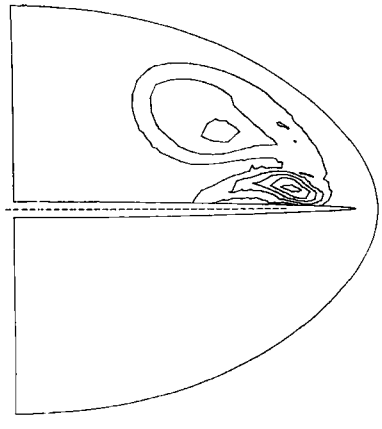

Wake
$x/c = 1.15$ (*b*)

FIGURE 12(*b*). For description see p. 305.

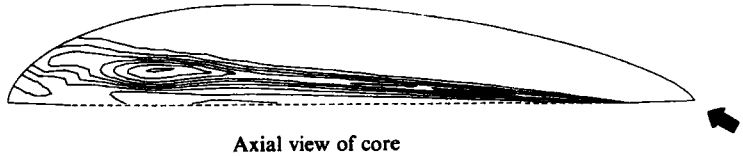

Axial view of core

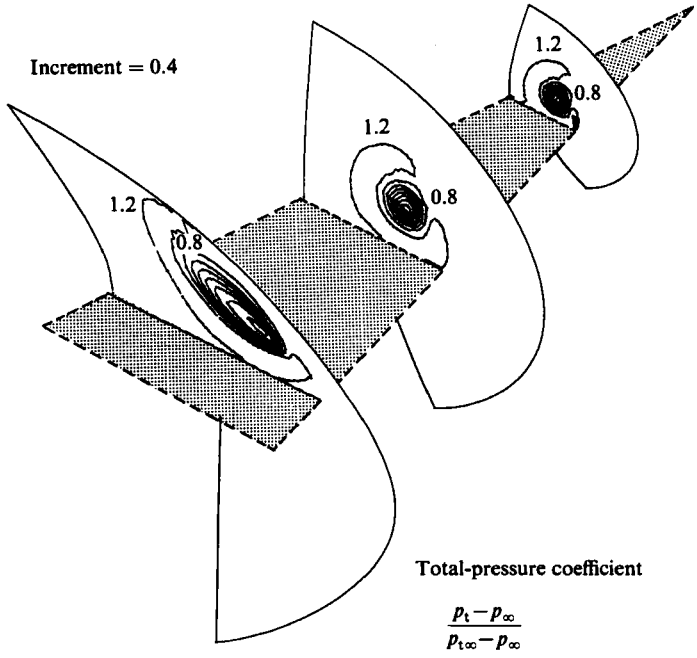

Total-pressure coefficient

$$\frac{p_t - p_\infty}{p_{t\infty} - p_\infty}$$

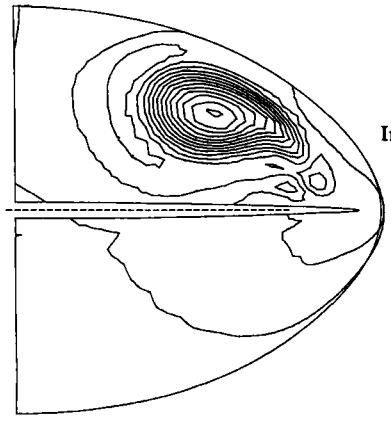

(*c*)

FIGURE 12(*c*). For description see p. 305.

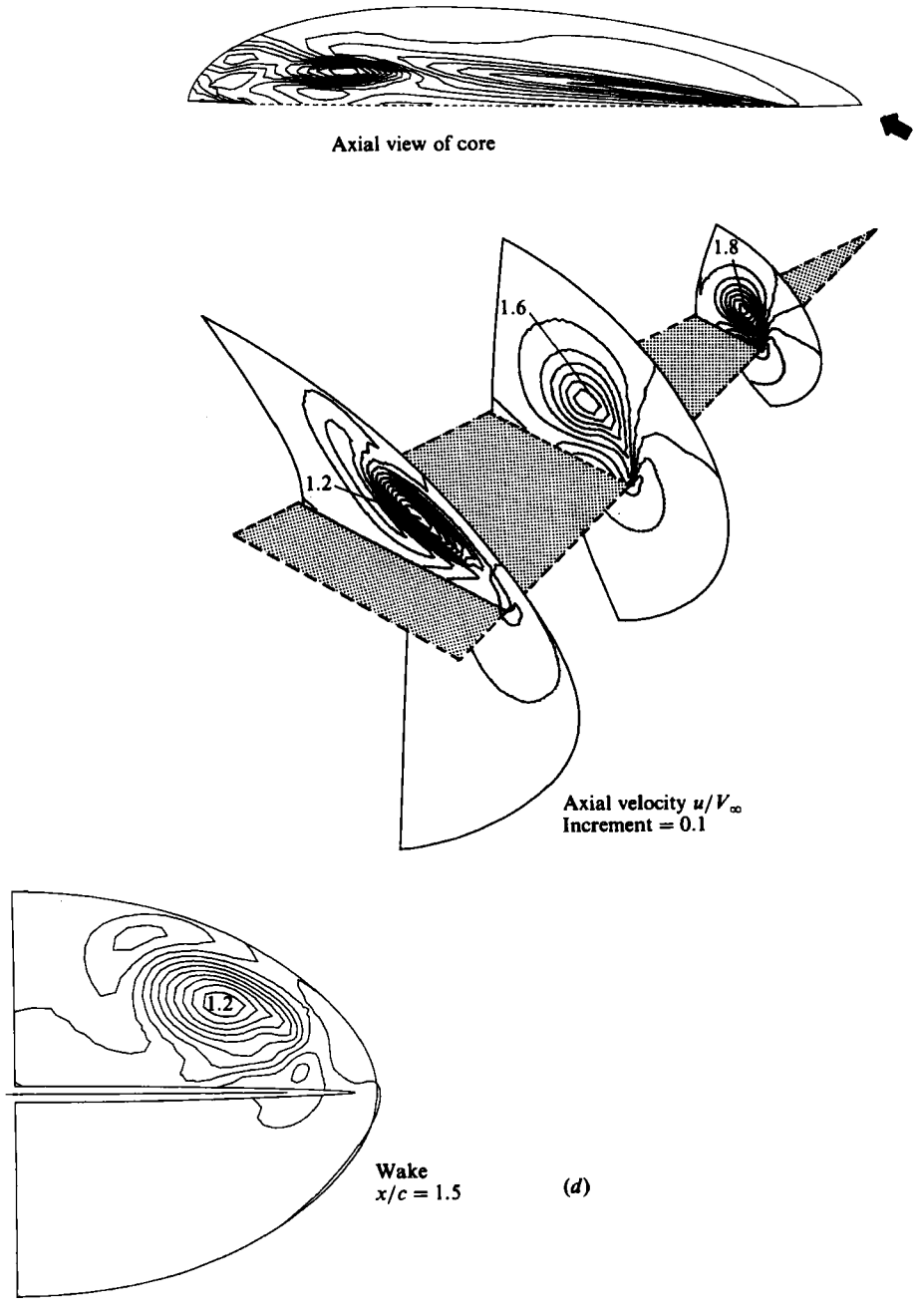

FIGURE 12(*d*). For description see opposite.

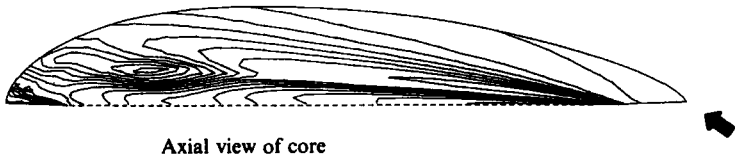

Axial view of core

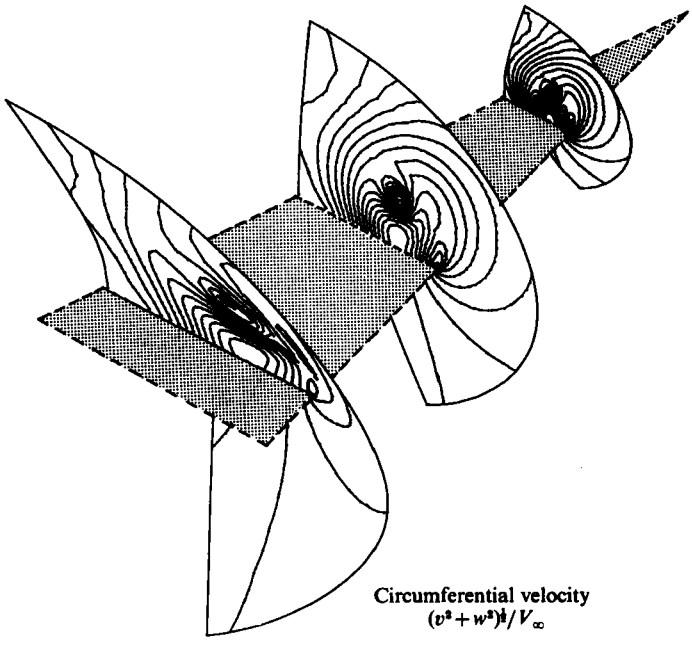

Circumferential velocity
$(v^2+w^2)^{\frac{1}{2}}/V_\infty$

Increment = 0.1

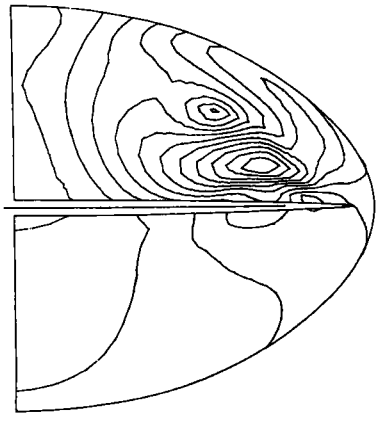

Wake
$x/c = 1.5$

(*e*)

FIGURE 12. The vortex flow field is surveyed by contour maps of the computed Euler-equation solution for flow past a 70° swept flat-plate delta wing. They are drawn in four non-planar mesh surfaces at the $x/c = 0.3$, 0.6, 0.9 and 1.15 stations and in one mesh surface which passes approximately through the axial core of the vortex. $M_\infty = 0$, $\alpha = 20°$. (*a*) Isobars of pressure coefficient C_p. (*b*) Vorticity magnitude contours $|\boldsymbol{\Omega}|$ increment = 0.02. (*c*) Contours of total-pressure coefficient $(p_t - p_\infty)/(p_{t\infty} - p_\infty)$, increment = 0.4. (*d*) Axial-velocity u/V_∞ contours, increment = 0.1. (*e*) Circumferential-velocity $(v^2+w^2)^{\frac{1}{2}}/V_\infty$ contours, increment = 0.1.

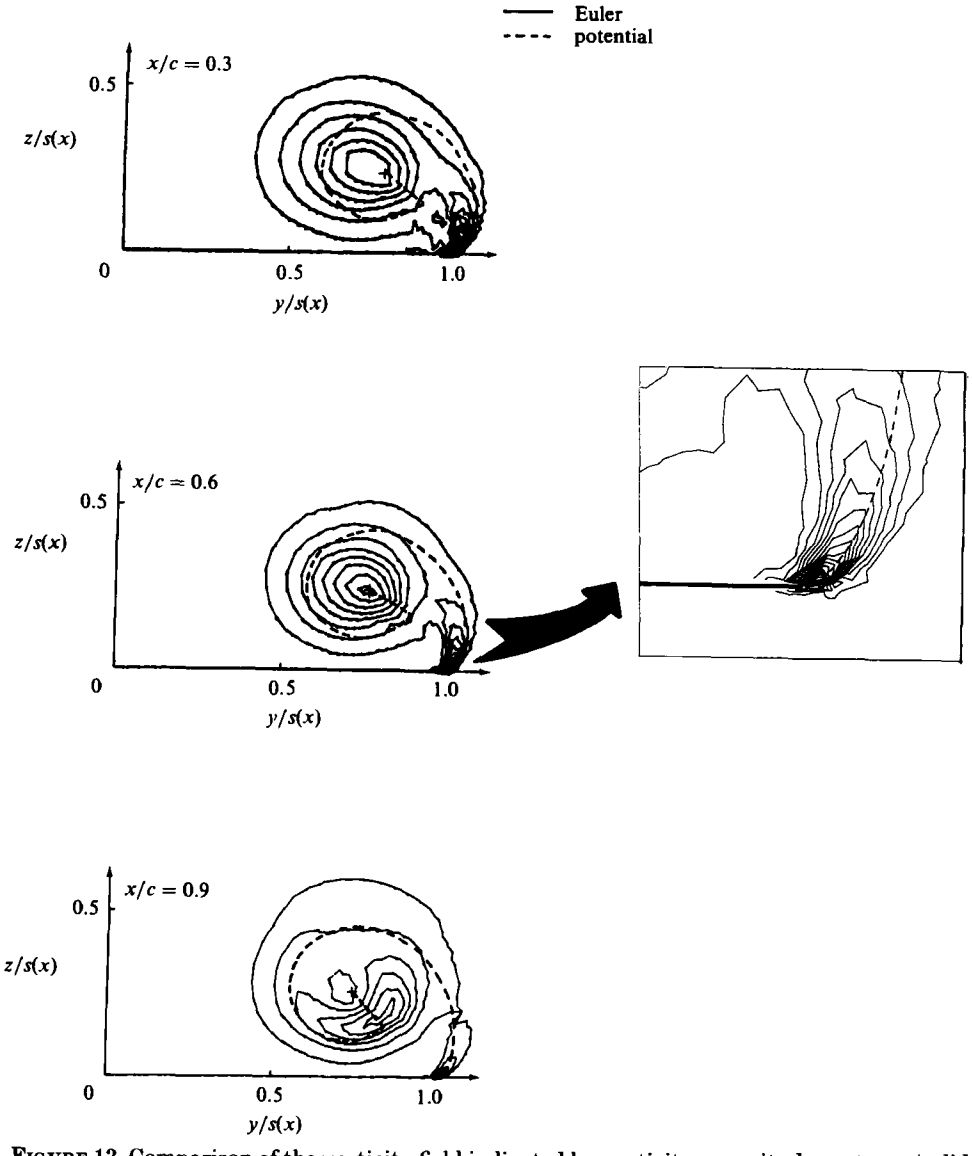

FIGURE 13. Comparison of the vorticity field indicated by vorticity-magnitude contours (solid lines) computed with the Euler equations and the shed vortex (dashed lines) that is fitted as a discontinuity to the surrounding potential solution obtained by the 3-dimensional panel method. It shows good agreement on the vortex position.

Euler-equation solution indicates the same trend (see the enlargement of the leading-edge region in figure 13). The sheet appears to depart tangentially from the lower surface of the leading edge. This comparison is the first quantitative demonstration so far that a vortex sheet separating from a swept leading edge can be captured in the vorticity field of the Euler-equation solution with a reasonable degree of realism. The curious distortion of the contours in the $x/c = 0.9$ station and the associated second island of vorticity is another indication of the additional vortex emanating from the sheet as discussed above.

An informative, and usually qualitative, manner to examine a flow over a wing is to look at its isograms on the wing surface. In figure 14 (*a–d*) we present such views together with the more quantitative graphs of spanwise distributions at three x/c = constant stations and compare them with the potential values available to us. In both sets of computed isobars (figure 14*a*) the pressure trough under the leading-edge vortex has about the same shape, position and width, and the two agree rather well except for minor differences appearing along the plane of symmetry and at the tip due to the difference in the local geometry there. The peak level of the suction along the entire trough on the upper surface is somewhat lower in the Euler results, and shifted slightly inboard at $x/c = 0.3$, following the trend we saw in figure 13. The enlargement of the apex region, however, demonstrates that the Euler solution is not conical just downstream of the apex. The potential flow is mildly singular at this point, but it seems that the large gradients occurring there cannot be fully resolved in the Euler solution. This follows from the property of the finite-volume scheme that at a mesh singularity like the apex or leading edge it loses accuracy (but not stability). We observe that the vortex flow in this solution needs about 3.5% chord lengths, corresponding to 5 or 6 cells in the stream direction, to build up the suction peak and attain its minimum C_p contour of -3.2. The contours of total-pressure coefficient in figure 14 (*b*) confirm this explanation. The largest losses, even negative values, are found near the apex. At $x/c = 0.002$ both upper and lower surface suffer heavy losses, by $x/c = 0.035$ the lower surface has recovered but the upper surface shows a mix of both loss and gain, which swings entirely to gain further downstream, the largest being at $x/c = 0.3$. This probably accounts for the inboard shift of the vortex at $x/c = 0.3$. Figure 14 (*b*) therefore serves as a calibration of computed errors in total pressure, i.e., even with this level of error locally, a reasonably accurate flow field is obtained overall, by comparison with the potential results. We have found, however, that, the more we restrict the region where the largest losses occur to the immediate neighbourhood of the apex by condensing the mesh cells there, the better the solution is on the remainder of the wing.

The axial, u/V_∞, and circumferential, $(v^2+w^2)^{\frac{1}{2}}/V_\infty$, velocity components on the upper surface are displayed in figure 14 (*c, d*). The potential flow attaches to the wing at the plane of symmetry and moves in the outboard direction along the entire upper surface. In the Euler solution the attachment point on the aft part of the wing is not in the plane of symmetry but at a position between 15 and 25% semispan. Outboard of this location the flow is toward the leading edge and, inboard of it, toward the plane of symmetry.

4. Concluding remarks

The artificial-compressibility method is an interesting one for solving the incompressible Euler equations because it is equally applicable in two- or three-dimensional problems and because its solutions provide a lot of insight into the types of flows that can occur. A free parameter can be chosen to alter the wave-propagation speeds, and unexpected transient discontinuities have been described which may play a role in the vorticity-creation mechanism. In a 2-dimensional flow field vorticity was observed to evolve in time, culminating in a steady flow with circulation. A steady 3-dimensional flow field with a free-shear layer has also been computed and its features have been discussed. Comparison with an accepted solution was reasonable; even large (but local) errors in total pressure do not seriously degrade the global

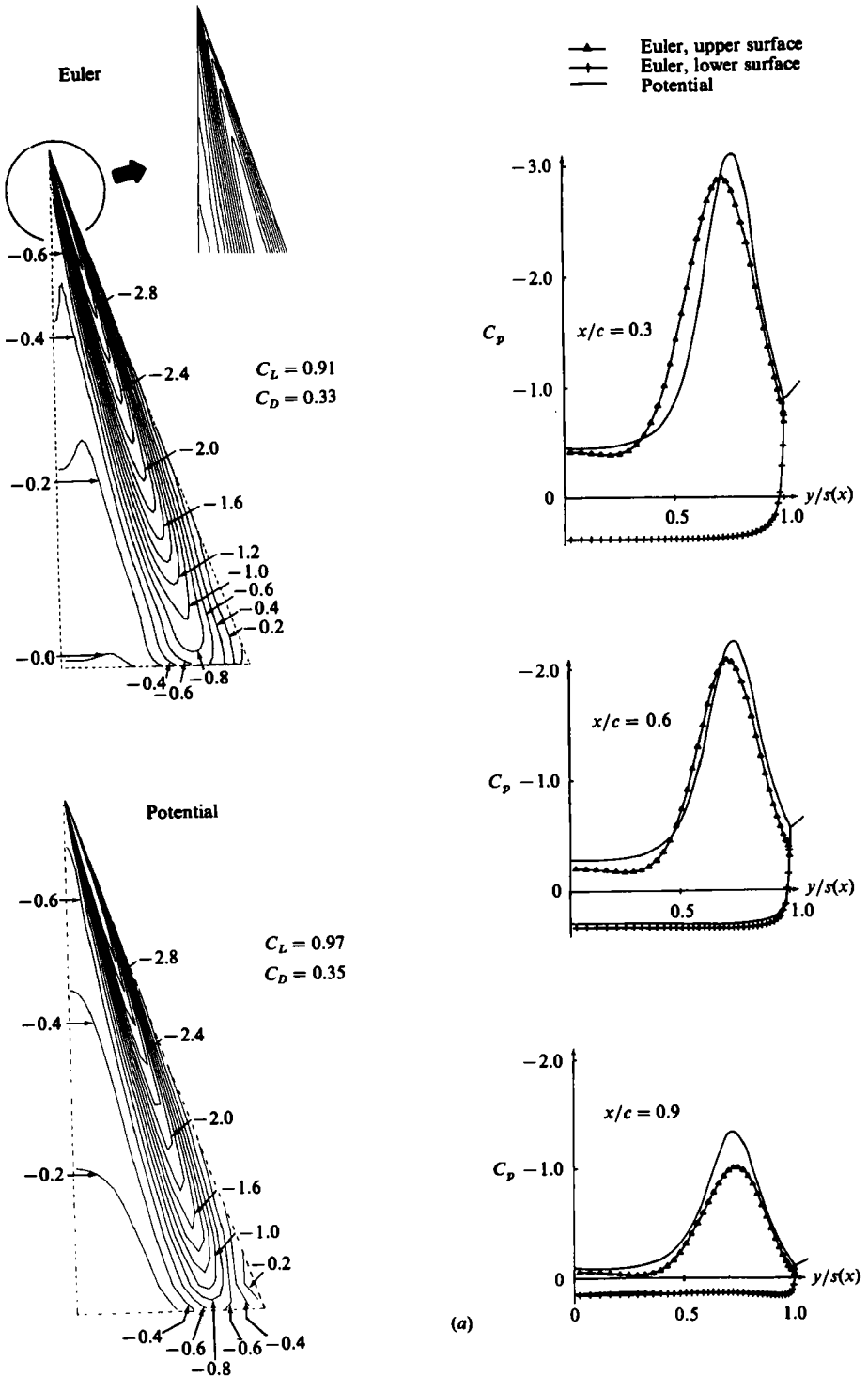

FIGURE 14(a). For description see p. 311.

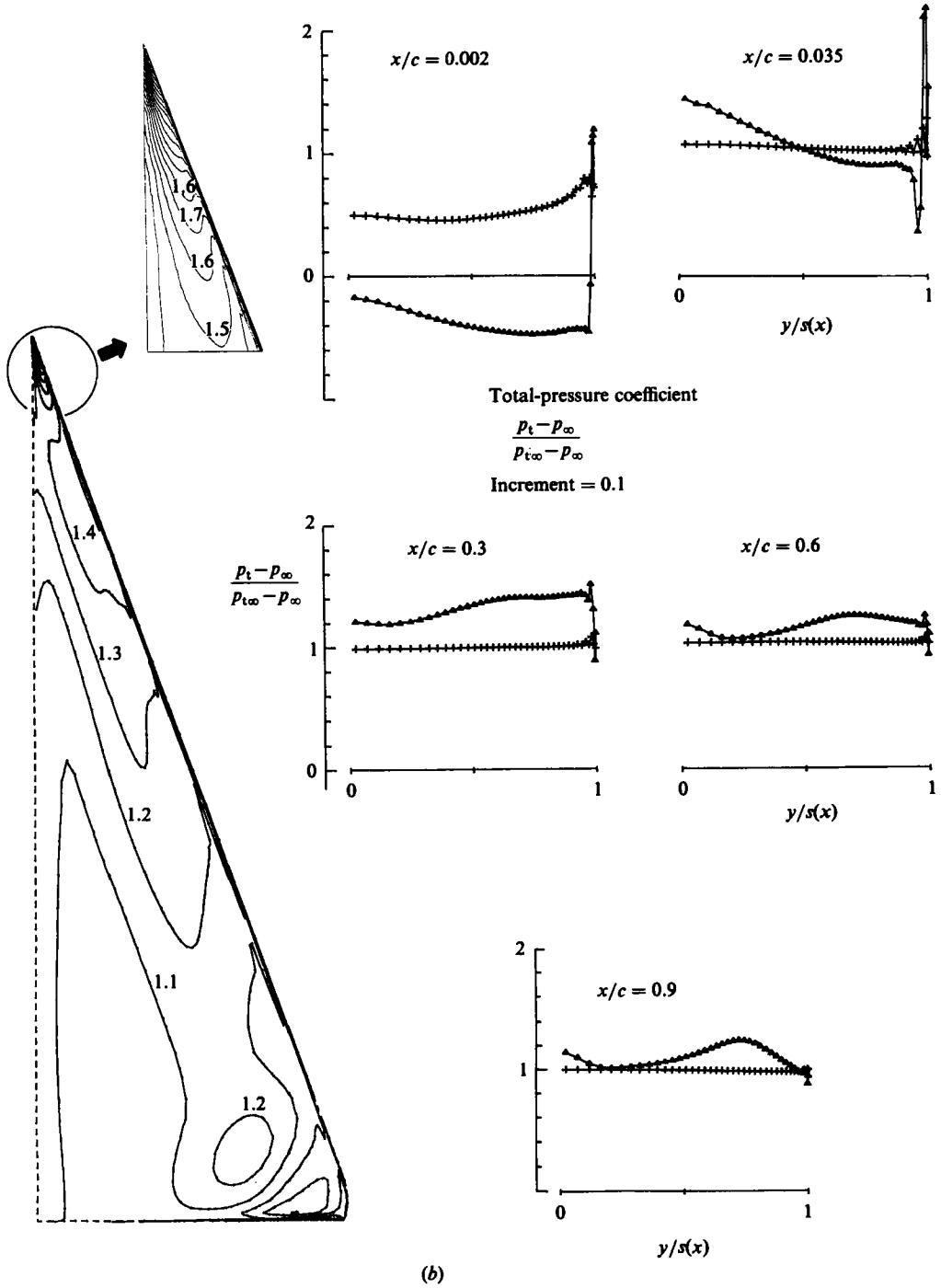

(*b*)

FIGURE 14 (*b*). For description see p. 311.

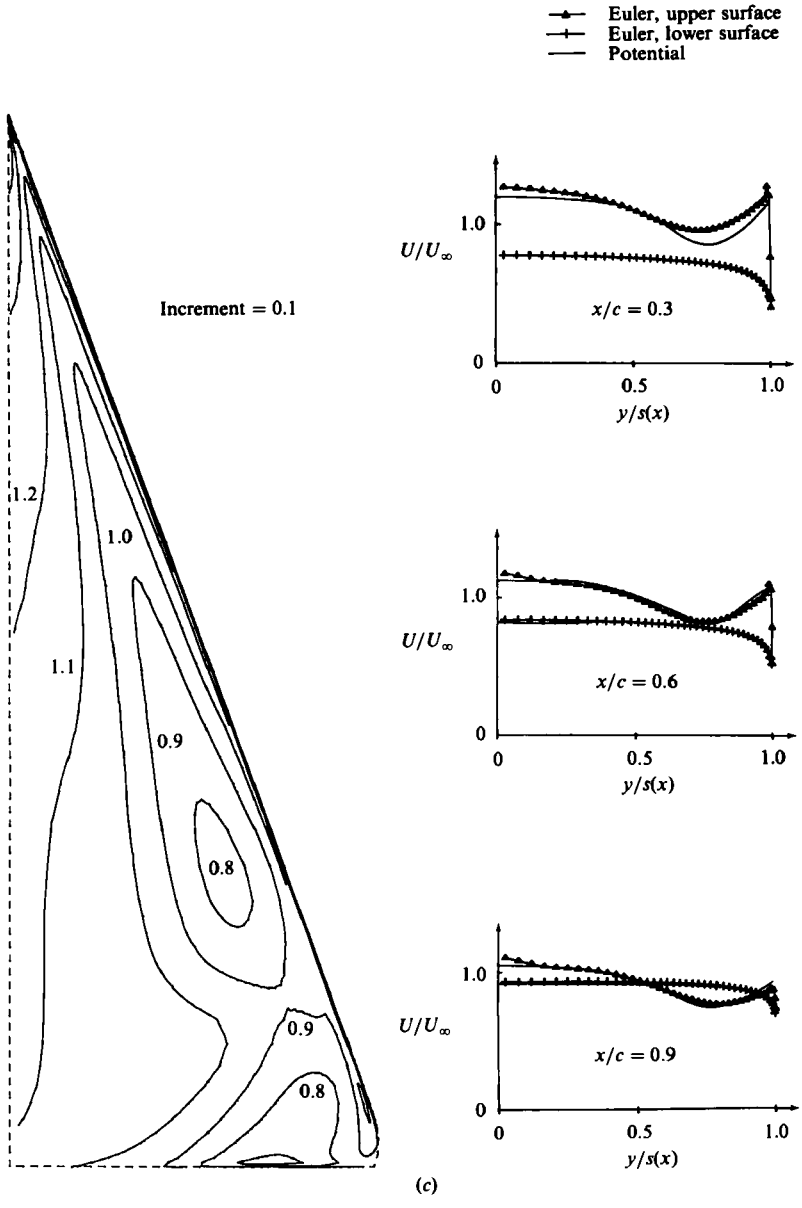

(*c*)

FIGURE 14(*c*). For description see opposite.

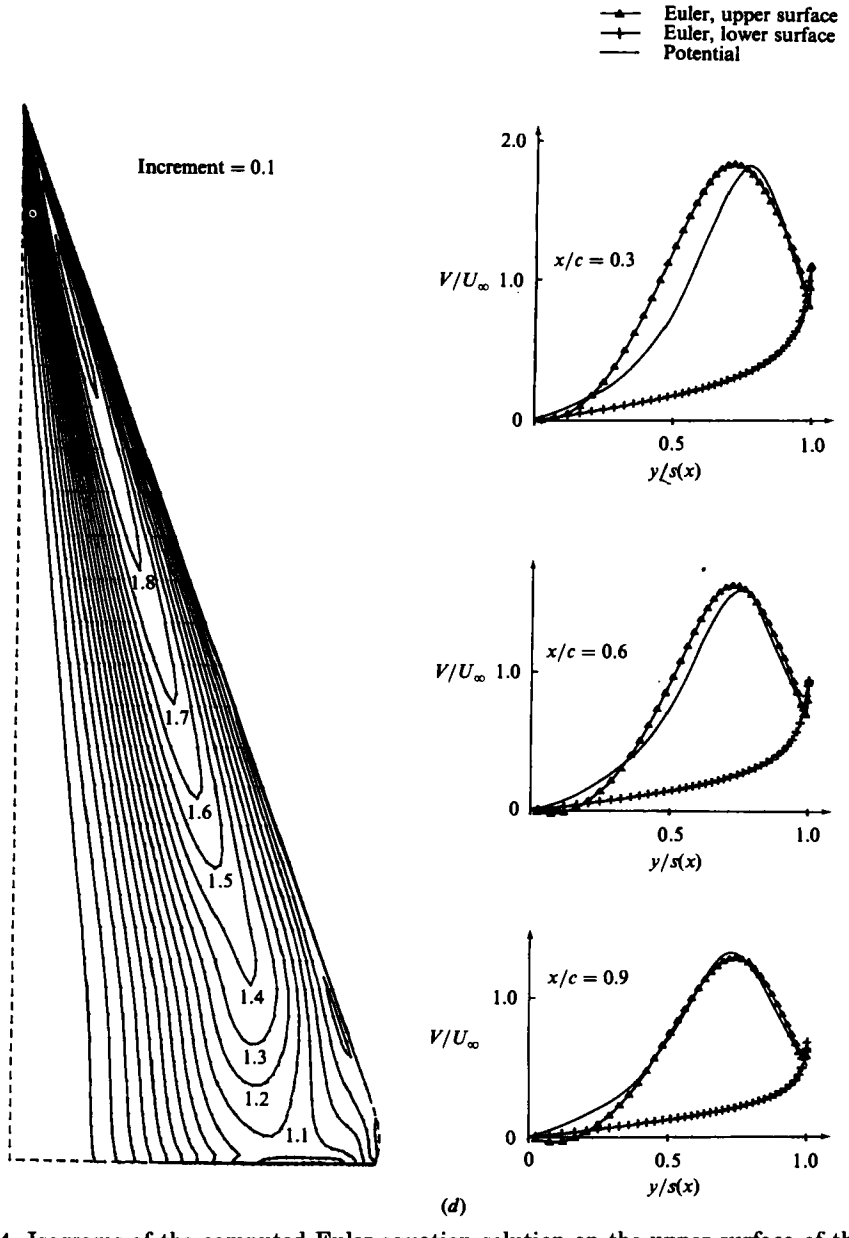

FIGURE 14. Isograms of the computed Euler-equation solution on the upper surface of the wing together with three corresponding graphs versus local semispan at $x/c = 0.3, 0.6$ and 0.9. 70° swept flat-plate delta wing. $\alpha = 20°$. (*a*) Isobars of pressure coefficient C_p compared with the potential solution, increment = 0.2. (*b*) Contours of total-pressure coefficient $(p_t - p_\infty)/(p_{t_\infty} - p_\infty)$, increment = 0.4. (*c*) Axial-velocity u/V_∞ contours and spanwise graphs compared with the potential solution, increment = 0.1. (*d*) Circumferential velocity $(v^2 + w^2)^{\frac{1}{2}}/V_\infty$ contours and spanwise graphs compared with the potential solution.

accuracy, and a curious vortex-like phenomenon was seen to develop just ahead of the trailing edge. This feature may arise from a disturbance of the leading-edge sheet or it may be associated with the roll-up of the trailing-edge sheet. A more definite explanation must await further investigation.

We wish to thank Harry Hoeijmakers at NLR for many helpful discussions and insight and Control Data Corporation for providing us with computer time for the further development of this method.

REFERENCES

CHORIN, A. J. 1967 A numerical method for solving incompressible viscous flow problems. *J. Comp. Phys.* **2**, 12–26.

ENGQVIST, B. & MAJDA, A. 1977 Absorbing boundary conditions for the numerical simulation of waves. *Math. Comp.* **31**, 629–651.

ERIKSSON, L.-E. 1975 Calculation of two-dimensional potential flow wall interference for multicomponent airfoils in closed low speed wind tunnels. *FFA TN* AU-1116, Part 1, *Stockholm.*

ERIKSSON, L.-E. 1982 Generation of boundary-conforming grids around wing–body configurations using transfinite interpolation. *AIAA J.* **20**, 1313–1320.

ERIKSSON, L.-E. 1984 Boundary conditions for artificial dissipation operators. *FFA TN* 1984-53, *Stockholm.*

ERIKSSON, L.-E. & RIZZI, A. 1983 Computer-aided analysis of the convergence to steady state of a discrete approximation to the Euler equations. *AIAA Paper* 83-1951 *presented at 6th CFD Conf., Danvers, MA.* (also *J. Comp. Phys.*, in press).

ERIKSSON, L.-E., RIZZI, A. & THERRE, J. P. 1984 Numerical solutions of the steady incompressible Euler equations applied to water turbines. *AIAA Paper* 84-2145.

HOEIJMAKERS, H. W. M. & RIZZI, A. 1984 Vortex-fitted potential solution compared with vortex-captured Euler solution for delta wing with leading edge vortex separation. *AIAA Paper* 84-2144.

HOEIJMAKERS, H. W. M. & VAATSTRA, W. 1973 A higher-order panel method applied to vortex-sheet roll-up. *AIAA J.* **21**, 516–523.

HOEIJMAKERS, H. W. M., VAATSTRA, W. & VERHAAGEN, N. G. 1983 Vortex flow over delta and double-delta wings. *J. Aircraft* **21**, 000–000.

HUMMEL, D. 1979 On the vortex formation over a slender wing at large incidence. *AGARD CP*-247.

PEYRET, R. & TAYLOR, T. 1983 *Computational Methods for Fluid Flow.* Springer.

RIZZI, A. W. 1978 Numerical implementation of solid-body boundary conditions for the Euler equations. *Z. angew. Math. Mech.* **58**, 301–304.

RIZZI, A. & ERIKSSON, L.-E. 1984 Computation of flow around wings based on the Euler equations. *J. Fluid Mech.* **148**, 45–71.

RIZZI, A. & ERIKSSON, L.-E. 1985 Vortex-sheet capturing in numerical solutions of the incompressible Euler equations. *SIAM J. Sci. Stat. Comp.* (in press).

WAGNER, H. 1925 Über die Entstehung des dynamischen Auftriebes von Tragflügeln. *Z. angew. Math. Mech.* **5**, 17–35.